

***ON THE COMPACTION OF HARD METAL POWDERS***  
***Preliminary Experimental and Theoretical Studies***

**Michael Hehenberger**  
**Larsgunnar Nilsson**  
**Thomas Olofsson**

**Peter Samuelsson**  
**Ove Alm**



**UNIVERSITY OF LULEÅ**

ON THE COMPACTION OF HARD METAL POWDERS -  
PRELIMINARY EXPERIMENTAL AND THEORETICAL STUDIES

by

Michael Hehenberger <sup>1)</sup>, Peter Samuelson <sup>1)</sup>,  
Larsgunnar Nilsson <sup>2a)</sup>, Ove Alm <sup>2b)</sup>, and  
Thomas Olofsson <sup>2b)</sup>

1) SANDVIK AB  
Coromantfabriken  
BOX 42 056  
S-126 12 STOCKHOLM 42  
SWEDEN

2) University of Luleå  
S-951 87 LULEÅ  
SWEDEN

a) Division of Structural Engineering  
b) Division of Rock Mechanics

## PREFACE

Powder compaction is a key step in all processes for the production of cemented carbides. In view of the great importance of hard materials for its products, SANDVIK AB has decided to start some basic research into various aspects of the compaction of hard metal powder.

The research work presented in this report has been conducted as a collaboration between SANDVIK AB and the divisions of Structural Engineering and Rock Mechanics at the University of Luleå. Larsgunnar Nilsson has been responsible for coordination of the work carried out at Luleå University.

The present paper should be considered as a progress report on our ongoing common effort to get an idea about the deformation and stresses introduced into powder material during compaction. It summarizes background material and contains the results of a series of pilot tests.

ABSTRACT

Mechanical properties of hard metal powder during compaction are studied. Uniaxial, hydrostatic and triaxial tests are described and the results used to obtain points on load surfaces which characterize the elasto-plastic behaviour of the powder. A constitutive model of the "cap"-type is proposed and its implementation - along with frictional relations - into a finite element program is discussed.

CONTENTS

1. Introduction	p. 4
2. Review of Previous Theoretical and Experimental Work on Powder Compaction	p. 7
3. Experimental Studies	p. 12
3.1 Equipment and Experimental Techniques in the Present Work	p. 12
3.2 Experimental Results	p. 17
3.3 Construction of Loading Surfaces	p. 25
4. Theoretical Studies	p. 35
4.1 Constitutive Relations	p. 35
4.2 Frictional Relations	p. 46
4.3 Computational Aspects	p. 48
5. Discussion and Conclusion	p. 50
6. References	p. 52

## 1. INTRODUCTION

It seems to be exceedingly difficult to give a precise theoretical description of the behaviour of powder material under pressure. Powder simply does not fit any of the conventional material models which were developed to account for constitutive properties.

In an attempt to get at least an approximate description, one may start from two extreme points of view.

The first obvious standpoint would be to try to give a microscopic description of the particles or "granules", to characterize them by size, hardness, shape, etc. and to account for interparticle forces, frictional behaviour and the like. In fact, there have been numerous attempts [Torre (1948), Bockstiegel & Hewing (1965), Sjöberg et al (1977), Fischmeister et al (1978), Arzt & Fischmeister (1979)] in this direction, with many interesting results and conclusions. However, results on a microscopic level are only of limited value as long as it is not possible to extrapolate them to the macroscopic scale. So far, there seems to be no valid way of carrying out such an extrapolation, although some interesting work along these lines is under way [Cundall & Strack (1979)].

The second extreme point of view would be to neglect the microscopic structure and to treat the powder as a homogeneous continuum. The material properties are then no longer derived from microscopic behaviour of individual particles, but rather based on experimentally observed macroscopic properties.

As a consequence, theoretical models dealing with the interrelation of such properties typically contain parameters to be fitted to experiment. Therefore, they are to be used cautiously, whenever applied under conditions which differ significantly from the ones valid during the experimental tests.

The obvious way to proceed would be to describe the mechanical behaviour of our powder during compaction in terms of stresses, displacements and strains, i.e. to utilize the continuum mechanical approach.

The first step in any attempt to arrive at a mathematical description of the constitutive properties of hard metal powder has to be to carry out the necessary experimental tests. Based on the results, one may then try to develop a material model. In order to verify the validity of such a model, the corresponding continuum equations have to be solved. If one wants to deal with realistic boundary conditions, shapes and load cases, it will be necessary to resort to a computational rather than analytic treatment, e.g. using the Finite Element Method (FEM) [see e.g. Zienkiewicz (1977)].

This was in fact the way we decided to proceed, namely to start out with triaxial tests of powder specimen, to use the result to derive constitutive relations and, finally, to implement these relations into a finite element program of enough versatility to permit nonlinear analysis of both material and geometric types. Material nonlinearities arise because of the highly "plastic" behaviour of the powder, whereas geometric nonlinearities arise from large deformations during compaction.

Section 2 contains a brief summary of previous experimental as well as theoretical work on the compaction of powder materials.

In section 3 we discuss our experimental set-up and present the results obtained by means of uniaxial, hydrostatic and triaxial compression tests of cylindrical powder compacts.

Section 4 deals with the theoretical and computational aspects of our work. We take up possible constitutive relations for powder material and discuss the problem of friction between powder and die wall.

Finally, section 5 contains a discussion of our preliminary results along with conclusions of importance for our future work.



## 2. REVIEW OF PREVIOUS THEORETICAL AND EXPERIMENTAL WORK ON POWDER COMPACTION

---

In the present paper we concentrate on the continuum mechanical aspects of the powder compaction problem. We are therefore omitting a closer discussion of work related to its, although very important, microscopic (particle) aspects, as long as there is no obvious connection with the macroscopic properties we wish to describe.

One of the earliest attempts to establish an empirical relationship between compacting pressure and density of the compact was made by Walker (1923). Based on an analogy with Hooke's law he proposed

$$(2.1) \quad \ln P = -\frac{L}{D} + C$$

where  $P$  denotes the applied pressure and  $D$  is the "relative" density of the powder (i.e. the ratio between compacted density and theoretical limit density of a non-porous material).  $L$  and  $C$  are constants.

A similar expression was proposed by Balshin (1938), who applied fluid mechanical concepts in support of his formula.

However, no such simple relationship as (2.1) can possibly account for the empirical findings. Even if  $L$  and  $C$  are fitted to the specific powder material and experimental conditions under consideration, the fact remains that (2.1) leads to unphysical consequences: For high enough pressures  $P$ ,  $D$  will for any choice of constants  $L$  and  $C$  exceed its limiting value of one.

An expression which turned out to be quite popular among practitioners was proposed by Shapiro & Kolthoff (1947) and, independently, by Kinspicky (1948). It reads

$$(2.2) \quad \ln \frac{1}{1-D} = kP + C$$

As in (2.1),  $P$  and  $D$  denote pressure and relative density, respectively;  $k$  and  $C$  are constants. This equation adequately represents the compaction process over a limited range of applied pressures. It overestimates the densities both at very low and at very high pressures.

A theoretical explanation of (2.2) was attempted by Torre (1948), who proposed a microscopic model of a hollow metal sphere with negligible internal pressure, exposed to surrounding hydrostatic pressure. In this way he tried to represent pores in solid material. By assuming a rigid - perfectly plastic material - he arrived at (2.1) with

$$(2.3) \quad k = \frac{3}{2} \sigma_s ; C = 0$$

$\sigma_s$  being the upper yield stress of the material. Unfortunately, Torre's expression (2.3) does not agree with experimental evidence which, according to Heckel (1961), rather suggests

$$(2.4) \quad k = \frac{1}{3 \sigma_s}$$

Further, by setting the constant  $C$  equal to zero, a vanishing pressure  $P$  would imply a vanishing density.

Hewitt et al (1973) extended Torre's theory by introducing strain-hardening, which enabled them to quite accurately predict the compaction process for all but the very low and the very high pressure areas.

Many more curve-fitting models have been proposed, but none of them seems to be free from the drawbacks of the models described above.

Recently, attempts have been undertaken to describe the powder material in terms of relationships between stresses and strains, thereby utilizing the mathematical theories of elasticity and plasticity.

Early work in this field was done by Suh (1969), who proposed a yield-criterion to predict the plastic flow of a frictional work hardening granular material. His yield surface has the geometrical form of a revoluting lemniscate. Depending on the stress state, the material may undergo an increase or decrease in volume. In a hydrostatic state of stress pure volume decrease will occur. In a general loading situation, the surface will change in order to include the work hardening effect. Suh does not mention any comparisons with experimental results.

Another early proposal for a yield criterion is due to Kuhn & Downey (1971), who extended v. Mises' classical criterion by allowing the mean stress to influence yielding. When the density of the compact approaches the theoretical limit density, this dependence on the first stress invariant is gradually removed and v. Mises' criterion is recovered for the fully compacted body. The magnitude of the yield stress does not only depend on the deviatoric strains, but also on the degree of densification. The relation between stress and strain is determined by a normality flow rule.

Kuhn & Downey tried to verify their theory using iron powder samples of varying densities. The samples were fitted into a die and an axial load was applied. By measuring the axial stresses and strains, the density was calculated for incremental deformation steps. Except for high stresses, the formal agreement was good. Even for experimental data due to Antes (1970), who reported homogeneous compression and plain strain compression tests on sintered compacts from different iron powders, a reasonable agreement was found except for high stresses.

Theoretical work on plasticity models suitable for powder material has been carried out at many places - among them notably the USSR and Japan - during the past two decades. However, there seems to be a general lack of empirical support for these models. In other words, the effort spent to do careful testing and to perform experimental verifications most often did not match the mathematical sophistication of the models. For practical purposes, simple empirical relationships as the ones discussed at the beginning of this section, despite their often serious principal drawbacks are still more useful. It appears therefore that real progress in this field only can be made by a united effort in the experimental, theoretical and computational fields.

Such an effort has recently been initiated by the Philips Research Laboratories, Eindhoven, The Netherlands. Philips has during the past five years developed an impressive setup of advanced test equipment for, in particular, ceramic powders.

The equipment consists of: (i) a triaxial cell for the accurate measurement of axial and volumetric strains of cylindrical specimen (Meerman & Knaapen (1979)), (ii) an apparatus for the measurement of the friction between powder and die wall (Strijbos (1977), Strijbos et al (1977)), (iii) an X-ray radiographic instrument with subsequent computer-controlled microdensitometric evaluation of the exposed X-ray film for the accurate measurement of density variations in pressed products (Broese van Groenou & Knaapen (1980)).

In collaboration with the geotechnical laboratory of Delft University of Technology, Philips has also undertaken some computational studies, based on an extension of the Mohr-Coulomb type of yield surface (Strijbos et al (1979), Vermeer (1980)).

Excellent reviews of the work by the Philips group were given by Broese van Groenou (1978, 1980) and by Strijbos et al (1979). Although these studies are of great interest for our present project, they will have to be carried further in two main areas in order to be really useful for the understanding of hard metal powder compaction. Firstly, the tri-axial equipment used by Philips only allows hydrostatic pressures up to about 50 MPa, whereas a limit of 250 MPa would be desirable for our purposes. Secondly, the computational studies have so far been restricted to two-dimensional calculations of cylindrical test specimen, while our present work is aimed at the full treatment of realistic, three-dimensional powder compacts.

### 3. EXPERIMENTAL STUDIES

#### 3.1 Equipment and experimental techniques in the present work

This section deals with the experimental techniques used to appraise the mechanical properties of a standard grade of hydrostatically pre-compacted SANDVIK hard metal powder. The following three types of tests were employed in order to determine the numerical values of the parameters entering the suggested constitutive equations of this material. (The symbols used in the text below are explained in figure 1. Compressive strains are assumed positive.)

- Uniaxial compression tests  $\sigma_1 > \sigma_2 = \sigma_3 = 0$
- Hydrostatic compression tests  $\sigma_1 = \sigma_2 = \sigma_3$
- Triaxial compression tests  $\sigma_1 > \sigma_2 = \sigma_3$

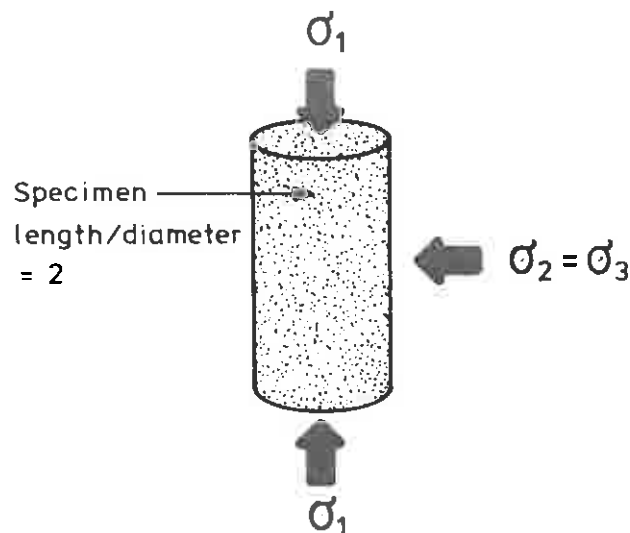


Fig. 1: Notation used in the text

An Instron, 500 KN universal testing machine, provided the necessary loading force in all our experiments. This machine can be operated in three different control modes: constant displacement rate, constant load rate, or it can be controlled by any user-selected transducer based on one or more strain gauges.

All our experiments were carried out at room temperature. The high-pressure tests were performed in a piston and cylinder apparatus (Fig. 2). The machine was controlled in the constant displacement rate mode in both the uniaxial and the hydrostatic compression tests. In the latter the specimen chamber ((4) in Fig. 2) was first filled with oil to a level well above the specimen. The top piston ((1) in Fig. 2) was then advanced downwards at a constant displacement rate, and thus we achieved an approximately constant rate of increase of oil pressure by 3.2 MPa/min.

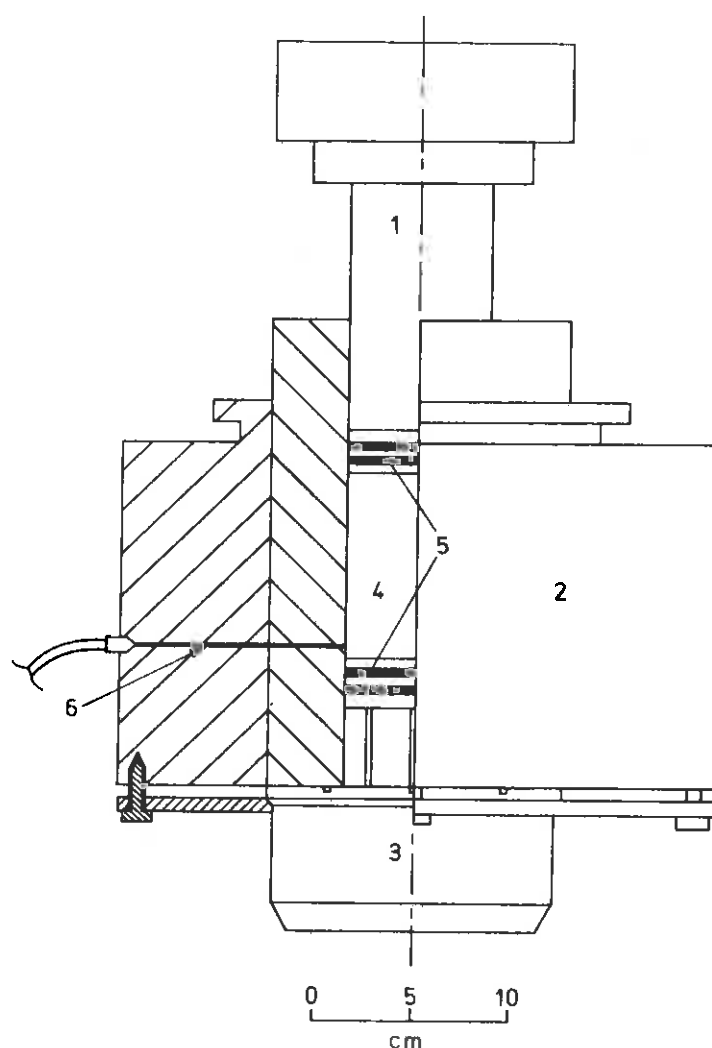


Fig. 2: Piston and cylinder apparatus; 1) top piston, 2) vessel, 3) bottom piston, 4) specimen chamber, 5) top and bottom o-ring seals, 6) confining pressure inlet (after Alm (1976))

The triaxial compression tests were somewhat more difficult to carry out because of the large deformations and small differential loads. To avoid large fluctuations in the load reading we found it necessary to control the confining pressure within 0.5 % over the pressure range 1-60 MPa. It was not possible to obtain such stability by adjusting the flow of oil through an ordinary constant pressure valve. We did, however, obtain an excellent pressure stability by using the signal from a pressure transducer (HBM P3M 200) as a feedback signal to the servo-controller of the Instron machine via a strain transducer conditioner. The differential load on the specimen was then obtained simply by opening the high pressure valve and letting out a small and steady flow of oil. The flow rate varied somewhat during the experiments and this caused small changes in the displacement rate. These variations were too small to have any significant effect on our results.

The top o-ring seal ((5) in Fig. 2) moves with the top piston. Friction between the seal and the cylindrical wall contributes to the readings such that we tend to over-estimate the load when increasing it and likewise, underestimate the load when decreasing it. Moreover, this friction becomes more pronounced with increasing oil pressure. This effect is clearly demonstrated in Fig. 9 (see p. 21), where each reversal of load direction causes the curve to drop fairly vertically, corresponding to the associated friction. Corrections based on these observations were therefore applied to the load readings in all the high-pressure experiments.

The cylindrical specimens, 60 mm long and 30 mm in diameter, were machined from hydrostatically pre-compacted hard metal powder. The specimens were



covered with latex rubber to prevent high-pressure fluid from penetrating into the specimens. Although the powder was pre-compacted, the specimens were highly porous and large deformations ( $\sim 25\%$ ) took place during the experiments. This made it impossible to measure the strains by conventional strain-gauge techniques. A new equipment for measuring large displacements was therefore designed. The deformation gauges which are shown in Fig. 3 were made of spring steel blades with strain gauges fixed in positions to give maximum output. They were connected in such a way that changes in strain-gauge resistance caused by variations in temperature and confining pressure were balanced out. Despite the careful construction of the gauges, however, some pressure effects could not be balanced out. These were corrected for by subtracting the high-pressure readings obtained with no specimen in the gauges from the recorded data on the various specimens.



Fig. 3: Deformation gauges used in the experiments

The axial deformation was measured over the whole specimen length by means of three cantilevers fitted on the bottom steel plate. The upper ends of the

cantilevers rested on a  $45^\circ$  conical steel stamp placed on top of the specimen. When the specimen deformed, the top of the cantilevers moved horizontally outwards and indirectly registered the axial deformation. This gauge was calibrated by comparing the reading of the gauge with that of a precision displacement gauge (LVDT).

The radial deformation was measured by means of a triangular-shaped gauge that was fitted directly on the specimen. It was important to measure at half the cylinder height since friction between the specimen and the steel end plates affected the radial deformation near the ends (c.f. Fig. 4). A coarse calibration of this gauge was obtained from the readings of the gauge, when placed on three different aluminium cylinders with diameters  $28.0 \pm 0.01$ ,  $30.04 \pm 0.01$  and  $31.05 \pm 0.01$  mm, respectively. A finer calibration was accomplished by deforming these aluminium cylinders and comparing the readings with those of the strain gauges fixed on the cylinders.

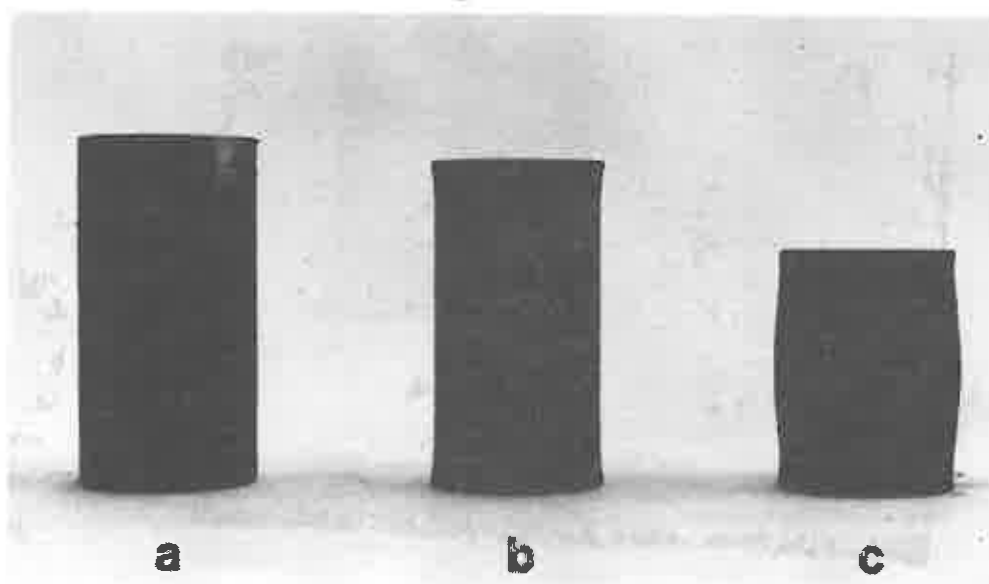


Fig. 4: The shape of the hard metal powder specimens: a) undeformed, b) after a hydrostatic compression test, c) after a triaxial compression test

The load was registered by the load cell of the Instron machine. The signals from the load cell and the deformation gauges were recorded on an analog Hewlett Packard 7046A X-Y recorder. The curves were then digitized on a Tektronix digitizer for quick and easy data evaluation and presentation. The experimental set-up is shown in Fig. 5.



Fig. 5: Experimental set-up

### 3.2 Experimental results

#### 3.2.1 Uniaxial compression tests ( $\sigma_1 > \sigma_2 = \sigma_3 = 0$ )

Cylindrical powder specimens with varying degrees of hydrostatic precompaction in the range 10-180 MPa were subjected to uniaxial loading. Both axial and radial strains were registered. A typical stress-strain diagram is presented in Fig. 6. In Fig. 7 we show the dependence of failure stress on the degree of precompaction or, more concisely, initial relative density which is defined with respect to the density after sintering.

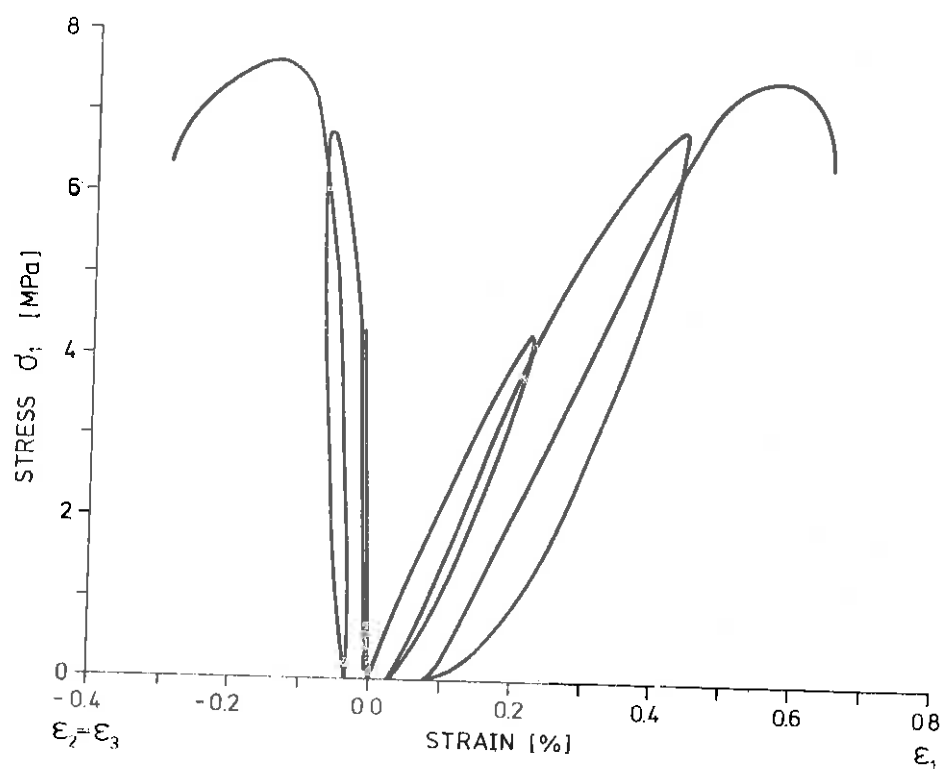


Fig. 6: Typical stress versus strain diagram from uniaxial compression tests; specimen pre-compacted to 40 MPa.

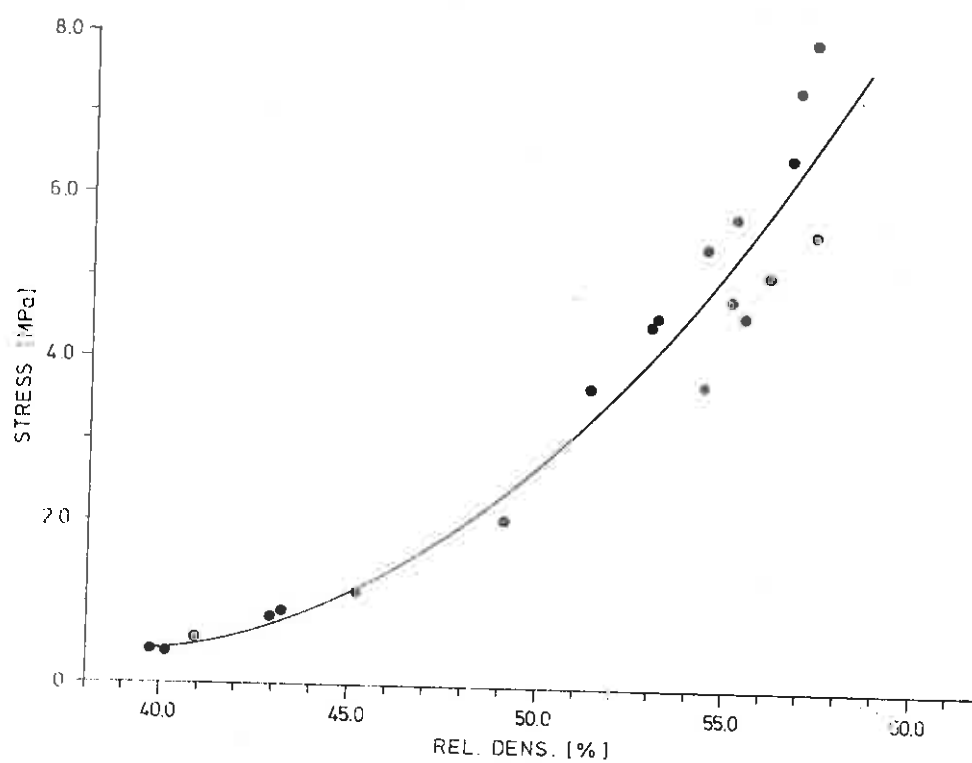


Fig. 7: Uniaxial failure stress versus relative density.

As expected, the failure stress increases for increasing initial densities. The scattering of data for relative densities above  $\sim 53\%$  ( $\sim 80$  MPa precompaction) can probably be attributed to defects like small cracks, to lack in parallelity of the test cylinder surfaces, and to end effects at the contact surfaces.

Different displacement rates in the range 0.004 to 40 mm/min were tried, but did not lead to any significant changes, except possibly to increase failure stresses for high displacement rates. By recording both axial and radial strains during unloading, it would be possible to obtain values for Young's modulus and Poisson's ratio for all degrees of precompaction. Due to insufficient resolution in our radial strain measurements, however, it turned out that we were unable to obtain accurate estimates of the latter. The dependence of Young's modulus on the relative density was similar to the behaviour of the failure stress, showing an increase for increasing density.

For relative densities in the range 39-57 % we obtained values of Young's modulus between  $\sim 300$  MPa and  $\sim 10,000$  MPa, whereas Poisson's number was estimated to lie around 0.15. Refined experimental techniques will be required to improve the accuracy of these figures.

### 3.2.2 Hydrostatic compression tests ( $\sigma_1 = \sigma_2 = \sigma_3$ )

Hydrostatic compression tests were carried out on 3 different degrees of pre-compaction: 10 MPa, 20 MPa, and 40 MPa. Before starting the planned series of tests, we studied the isotropy of the material. If the pre-compacted powder could be

considered as an isotropic material, we could reduce the strain measurements to record the axial shortening of the specimens only. Fig. 8 shows the hydrostatic pressure versus axial and radial strain for a specimen pre-compacted to 20 MPa. We observe that the curves differ slightly at large strains. Several explanations have been suggested for this difference, but we believe that it is mainly caused by disturbances at the three contacts between the gauge and the specimen. However, since this difference was small in relation to the total strain, we assume the material to be isotropic.

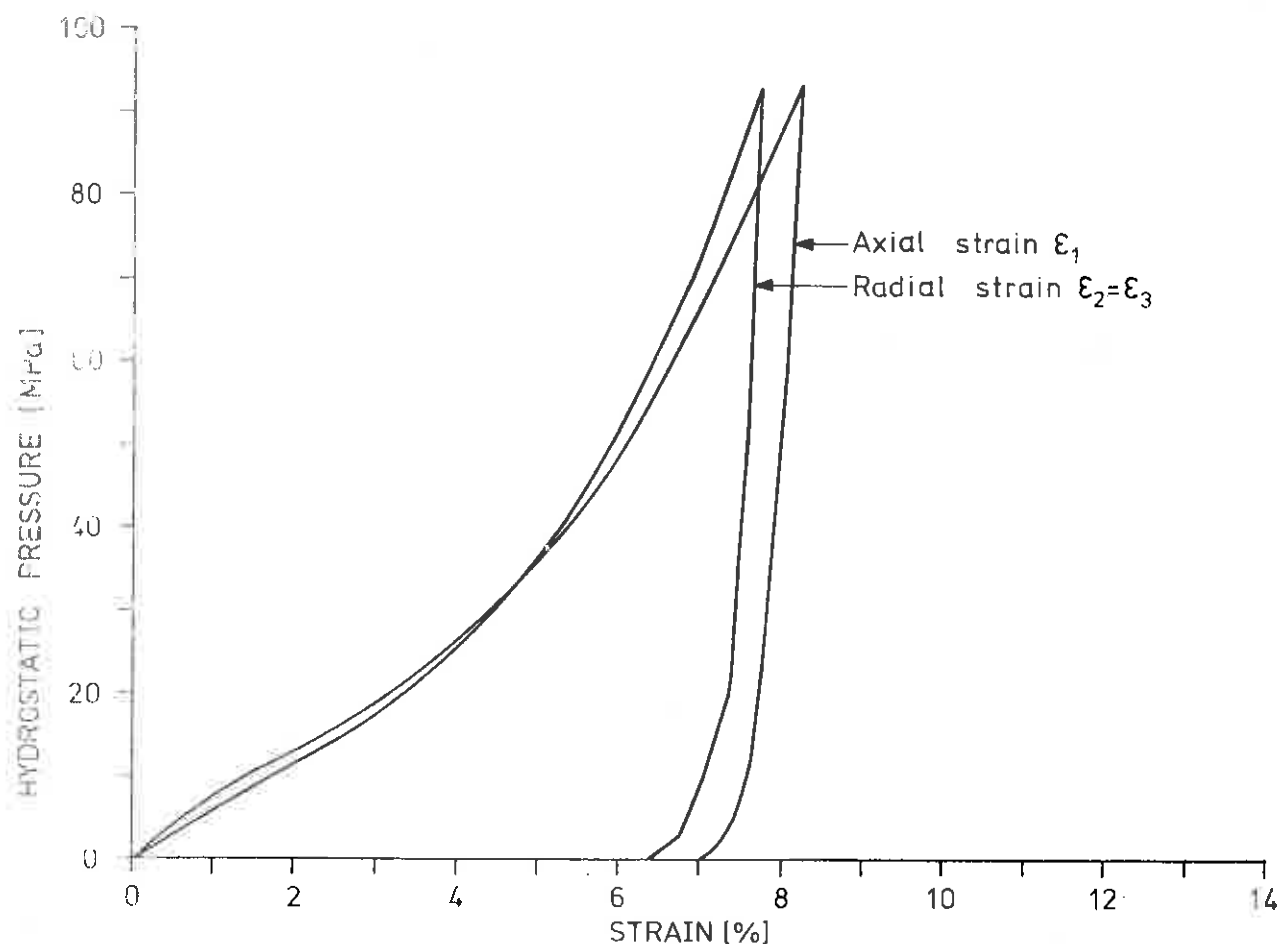


Fig. 8: Hydrostatic pressure versus axial and radial strain; specimen pre-compacted to 20 MPa.

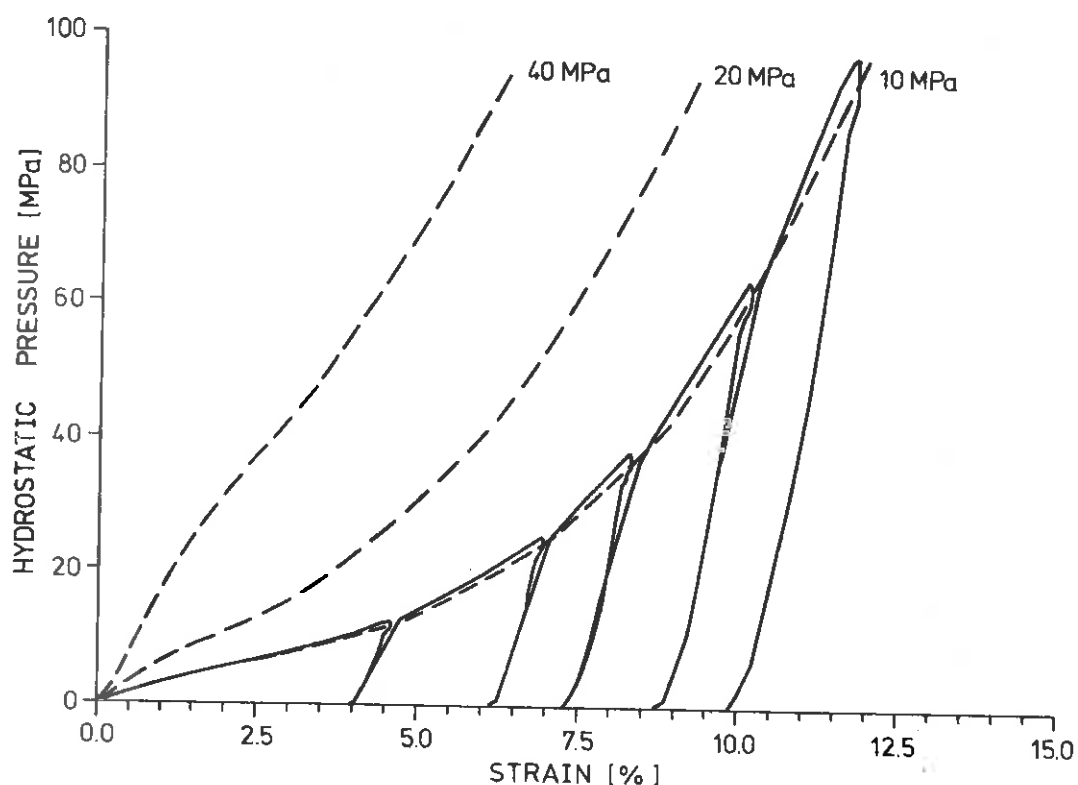


Fig. 9: Typical hydrostatic pressure versus axial strain diagrams for three degrees of pre-compaction, 10, 20, and 40 MPa (dashed curves; they are corrected for friction in the top seal). The solid curve is calculated from recorded data without any corrections.

The solid curve in Fig. 9 is an example of the typical relationship between hydrostatic pressure and axial strain for a specimen pre-compacted to 10 MPa. The dashed curves show typical results for the three degrees of pre-compaction after correction for friction in the top o-ring seal. The diagram also displays the response of the material to cyclic hydrostatic pressure. Typical data obtained in the hydrostatic experiments are summarized in Fig. 10. The small distortion of the cylindrical shape close to the end plates was neglected in the calculation of the densities.

In Fig. 10 we also show the "plastic" components

obtained by considering the strains remaining after unloading.

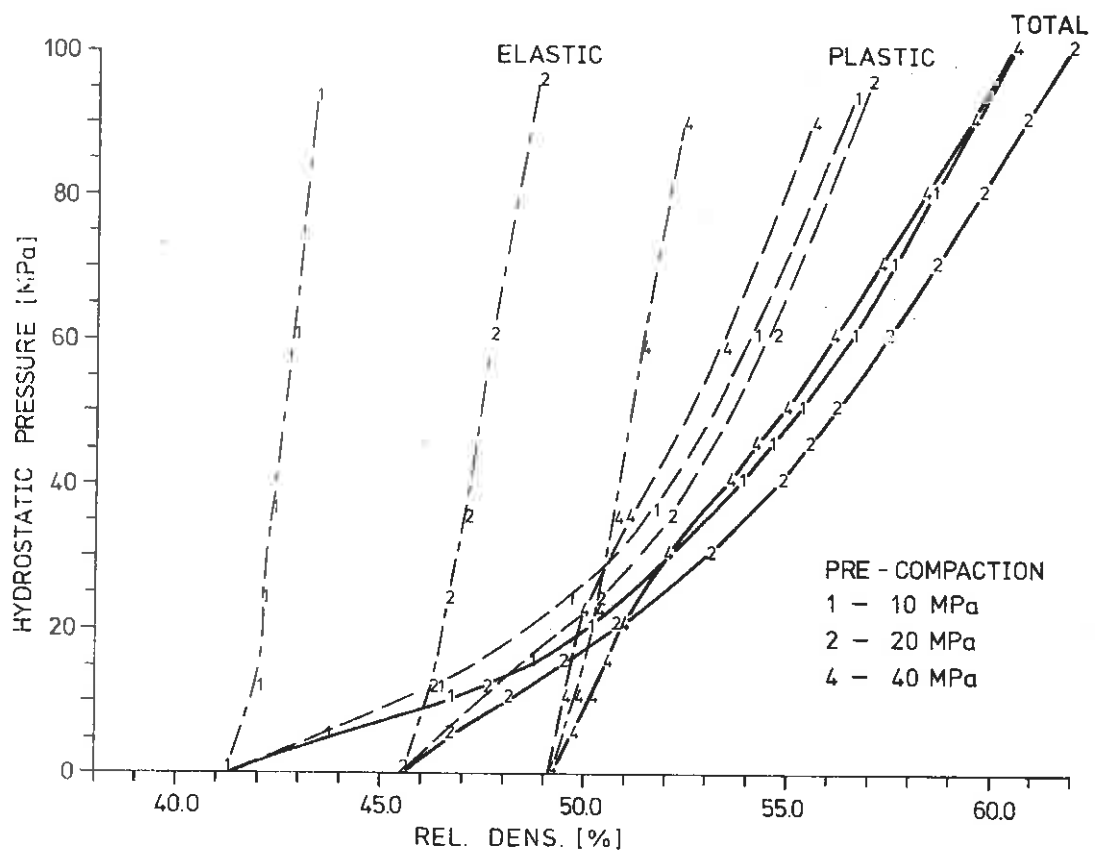


Fig. 10: Hydrostatic pressure versus relative density.

### 3.2.3 Triaxial compression tests ( $\sigma_1 > \sigma_2 = \sigma_3$ )

Triaxial compression tests were carried out at four different confining pressures, 15, 30, 45 and 60 MPa. The tests were performed on specimens pre-compacted to 10 MPa. The average displacement rate was  $1.5 \pm 1$  mm/min,



and the tests were stopped at approximately 35-40% total axial strain. The results of the triaxial tests are presented in Fig. 11. In order to facilitate a comparison, all strains are indicated relatively to the volumetric strains caused by the respective confining pressures. The total strains are therefore obtained by adding together the hydrostatic and the relative triaxial values.

As seen in Fig. 11, we performed cyclic loading and unloading tests at regular intervals to allow for the separation of elastic and plastic strain components.

In Fig. 12 we show the change of relative density for all four cases [ "A" : 15MPa; "B" : 30MPa; "C" : 45MPa; "D" : 60MPa ] . Contrary to Fig 11, the volumetric strains up to the confining pressure levels are taken into account. It is interesting to note how the curves bend back for sufficiently high differential stresses ( $\sigma_1 - \sigma_2$ ): At certain critical stress values, the increasing radial strains (radial expansion) more than outweigh the decreasing axial strains (axial compression). In other words, the volume starts to increase.

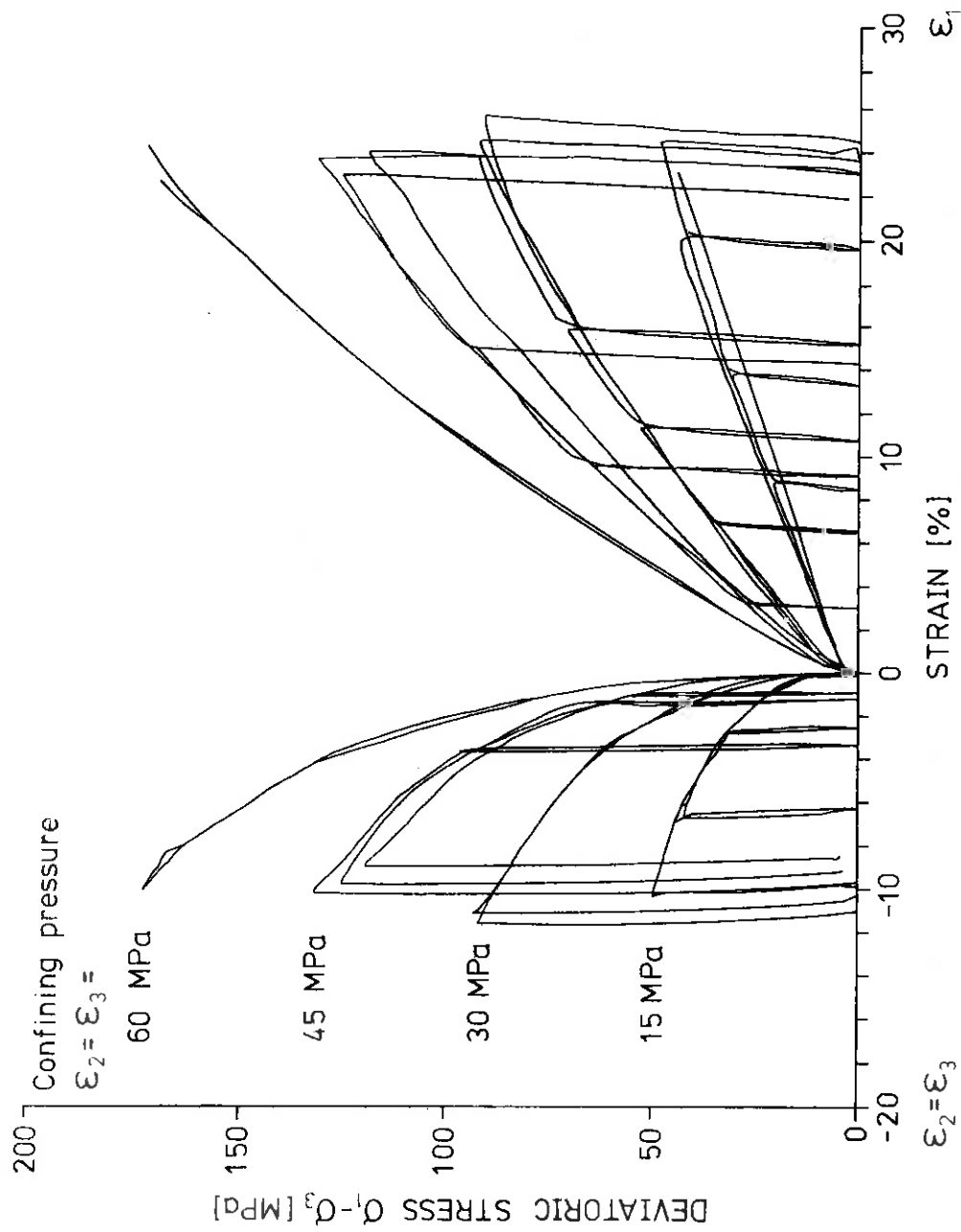


Fig. 11: Stress-strain curves from triaxial compression tests; all specimens precompacted to 10 MPa.

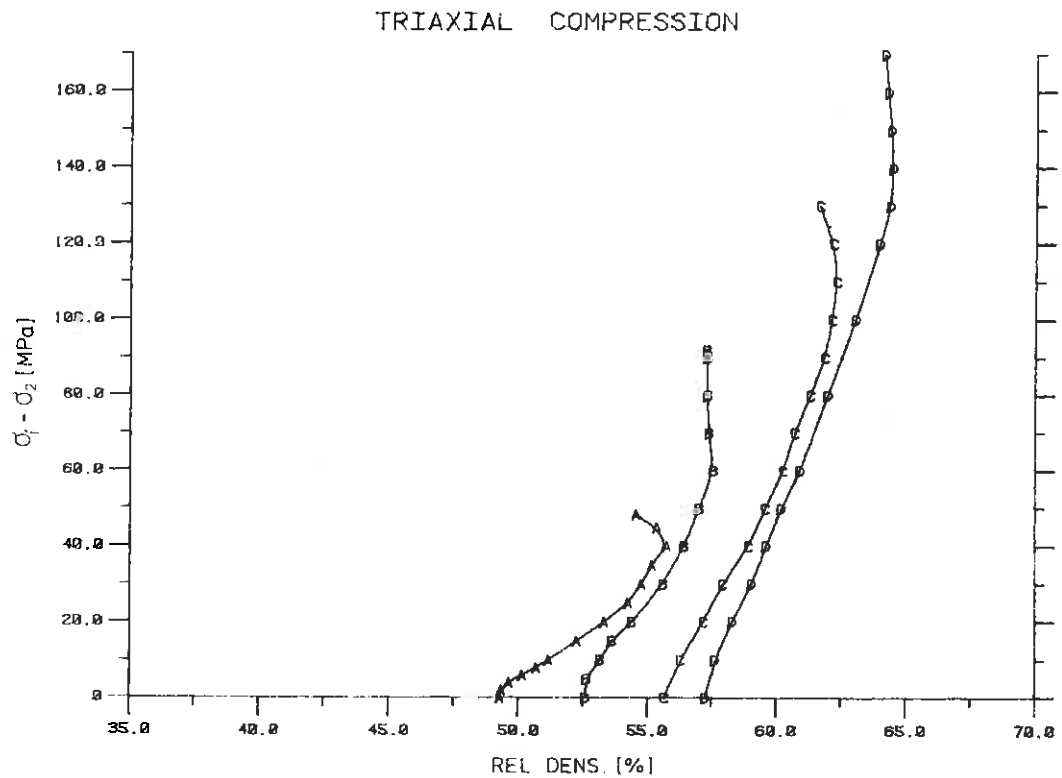


Fig. 12: Change of relative density during triaxial compression test. "A", "B", "C", "D" symbolize confining pressures 15, 30, 45, 60 MPa, respectively.

### 3.3 Construction of Loading Surfaces

When planning the tests described above, our aim was to provide data to be used in the formulation of a constitutive model for powder material. Due to our intention to rely on the classical flow theory of plasticity [see e.g. Malvern (1969)], our most important goal was the construction of loading surfaces based on uni-axial, hydrostatic, and triaxial tests.

A severe difficulty which we encountered was the question of definition of plastic flow for an unconventional material such as hard metal powder. We decided to employ well-defined strain hardening measures and to draw surfaces of constancy of these parameters.

Another key problem is the separation of elastic and plastic strain components. Plasticity theory requires the use of plastic components which may be obtained by subtracting the elastic components from the measured total strains. For our powder material, the plastic components dominate by far, and were taken to be the strains remaining after unloading (cf. p. 21-22, Fig. 10).

In the remainder of this section and in all figures shown below, whenever referring to "strain" we mean its plastic component. The results for confining pressure  $\sigma_2 = \sigma_3 = 60\text{MPa}$  (denoted by symbol "D"), for which unloading data were unavailable because of experimental difficulties, were obtained by straightforward extrapolation, based on the available information for confining pressures  $\sigma_2 = \sigma_3 = 15\text{ MPa}$  ("A"), 30 MPa ("B"), and 45 MPa ("C").

Convenient quantities for graphical display of our results as well as for the theoretical developments are the octahedral stresses and strains see e.g. Malvern (1969) or Kachanov (1971) . Denoting the direction of the cylindrical axis as "1"-direction and the radial directions as "2"- and "3"-directions, we obtain

$$(3.1) \quad \sigma_o = \frac{\sigma_1 + 2\sigma_2}{3}; \text{ Octahedral normal stress}$$

$$(3.2) \quad \tau_o = \frac{\sqrt{2}}{3} |\sigma_1 - \sigma_2|; \text{ Octahedral shear stress}$$

$$(3.3) \quad \epsilon_o = \frac{\epsilon_1 + 2\epsilon_2}{3} \quad \text{Octahedral normal strain}$$

$$(3.4) \quad \gamma_o = 2 \frac{\sqrt{2}}{3} |\epsilon_1 - \epsilon_2|; \text{ Octahedral shear strain}$$

In (3.3 - 4), the strains were taken to be the natural ones defined in the usual way as

$$(3.5 \text{ a}) \quad \epsilon = \ln \frac{L}{L_o} = \ln (1 + e_L)$$

where

$$(3.5 \text{ b}) \quad e = \frac{L - L_o}{L_o}$$

was the quantity registered by experiment and displayed e.g. in Fig. 11 (p. 24). For the large strains considered, the difference between natural and engineering strains is no longer negligible.

For the assumed and experimentally verified (c.f. Fig. 8, p. 20) isotropy of our material, the principal axes of the stress and strain spaces do coincide. The octahedral quantities defined above have then very similar meanings: With respect to an octahedral plane making the same angle with the three principal directions,  $\sigma_o (\epsilon_o)$  and  $\tau_o (\gamma_o/2)$  represent the normal and tangential components of the stress (strain vector). The relations with

the stress and strain invariants are given by

$$(3.6) \quad \sigma_o = \frac{1}{3} I_1 = \frac{1}{3} (\sigma_1 + \sigma_2 + \sigma_3)$$

$$(3.7) \quad \epsilon_o = \frac{1}{3} J_1 = \frac{1}{3} (\epsilon_1 + \epsilon_2 + \epsilon_3)$$

$$(3.8) \quad \tau_o = \sqrt{\frac{2}{3}} I_1' = \frac{1}{3} [(\sigma_1 - \sigma_2)^2 + (\sigma_2 - \sigma_3)^2 + (\sigma_3 - \sigma_1)^2]^{1/2}$$

$$(3.9) \quad \frac{\gamma_o}{2} = \sqrt{\frac{2}{3}} J_1' = \frac{1}{3} [(\epsilon_1 - \epsilon_2)^2 + (\epsilon_2 - \epsilon_3)^2 + (\epsilon_3 - \epsilon_1)^2]^{1/2}$$

and the lengths of the stress and strain vectors in the octahedral (Rendulic) plane are easily calculated to be

$$(3.10) \quad |\vec{S}_o| = [\sigma_o^2 + \tau_o^2]^{1/2}$$

$$(3.11) \quad E^* = |\vec{E}_o| = [\epsilon_o^2 + \left(\frac{\gamma_o}{2}\right)^2]^{1/2}$$

We have chosen to adopt  $E^*$  as defined by (3.11) as a convenient distortion measure (effective plastic strain) for the construction of load surfaces in octahedral stress space. For comparison, however, we also show two alternate families of surfaces based on the constancy of  $\epsilon_o$  and  $\gamma_o$ , respectively.

Before presenting the final figures, let us first consider how they were obtained.

Fig. 13 shows the first basic piece of information, the hydrostatic stress - (plastic) strain curve for a cylindrical specimen precompactd at 10 MPa.

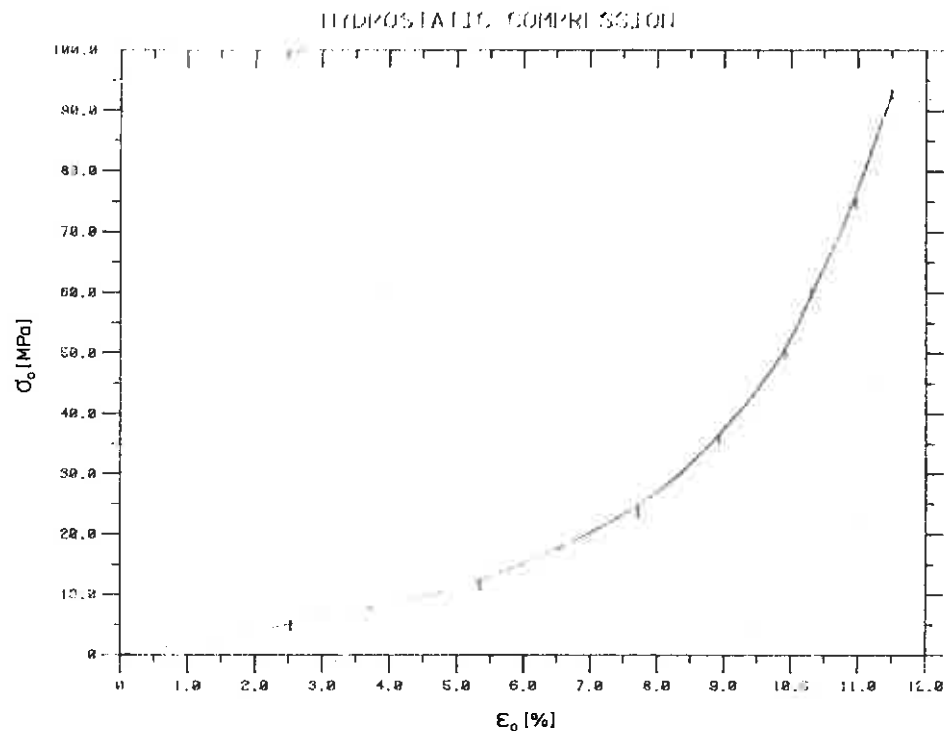


Fig. 13: Hydrostatic stress versus plastic octahedral strain.

In triaxial experiments, the situation is much more complicated and we have therefore chosen to display the interrelationships between the various quantities entering eqs. (3.1 - 11) in some detail.

Figs. 14 and 15 show the axial shortening as function of  $\sigma_0$  and  $\tau_0$ , respectively.

Figs. 16 and 17 show the increase of radial strain in the same situation. Note that the triaxial loading has been preceded by a hydrostatic compression up to the confining pressure, which has led to equal initial axial and radial strains. The same information as contained in Figs. 14-17 is displayed in an alternative fashion in Figs. 18-21. As seen, the decomposition into  $\epsilon_0$  and  $\gamma_0$  serves a very illustrative purpose.

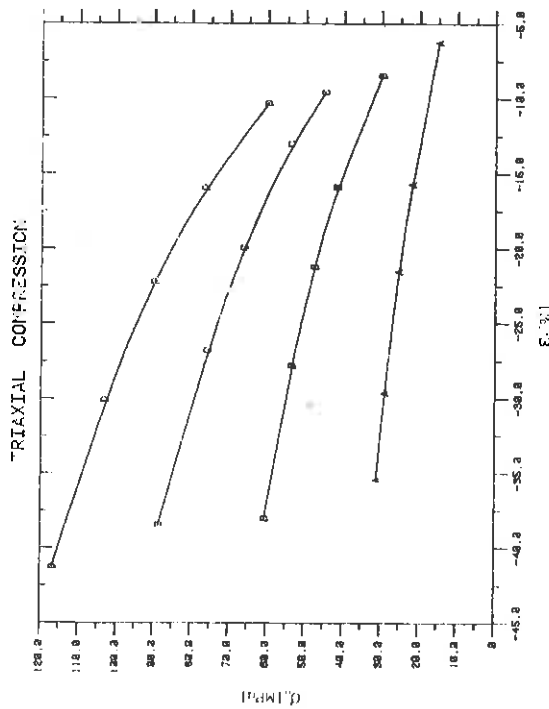


Fig. 14:  $\sigma_0$  versus axial strain  $\epsilon_1$

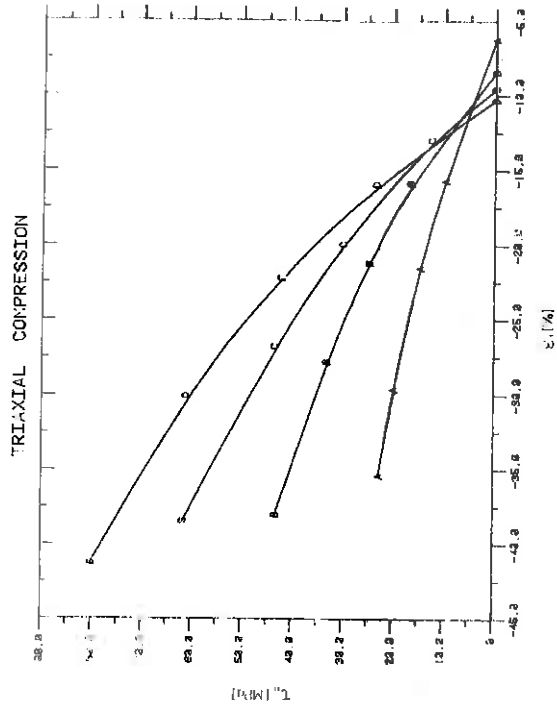


Fig. 15:  $\tau_0$  versus axial strain  $\epsilon_1$

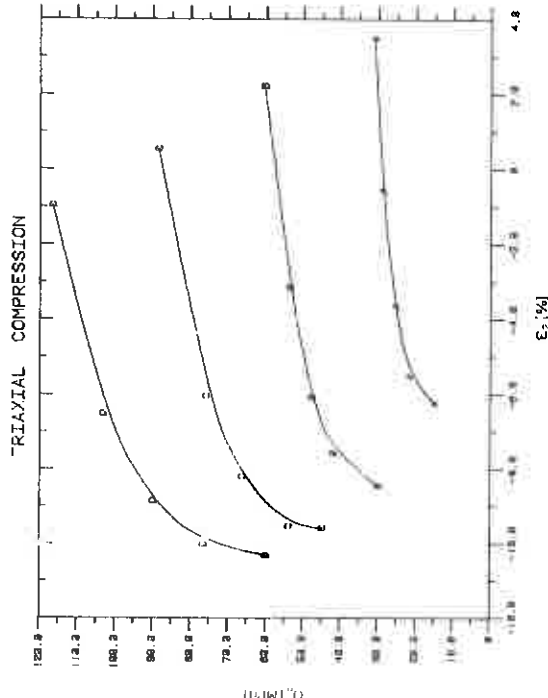


Fig. 16:  $\sigma_0$  versus radial strain  $\epsilon_2$

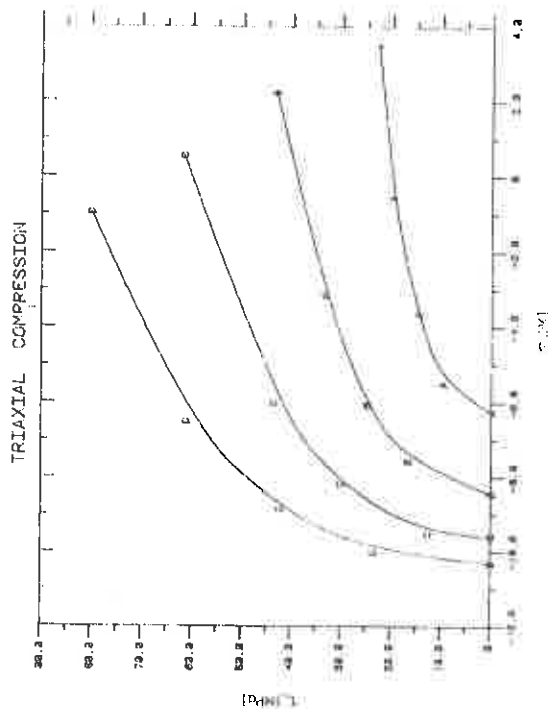
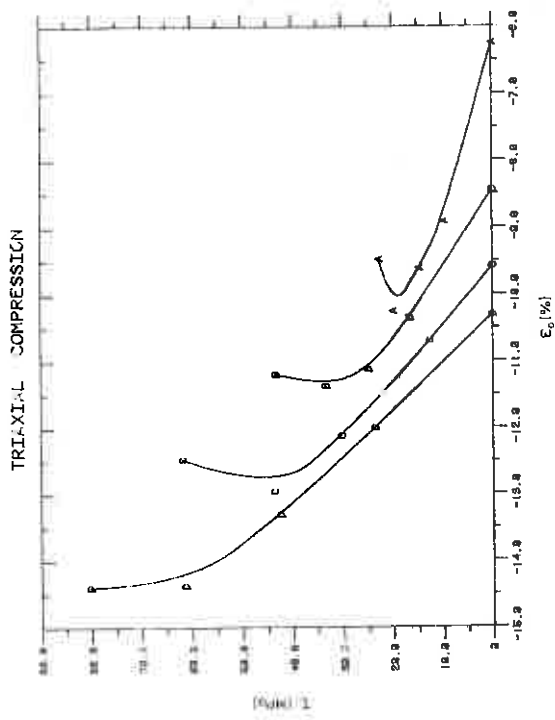
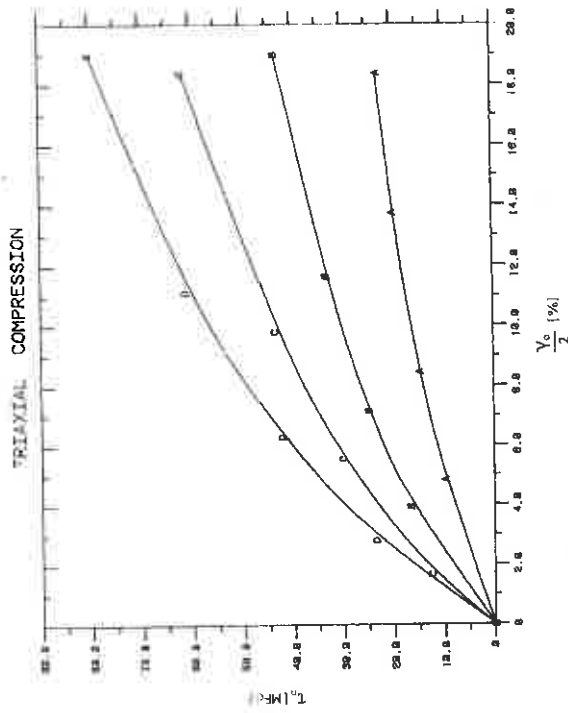
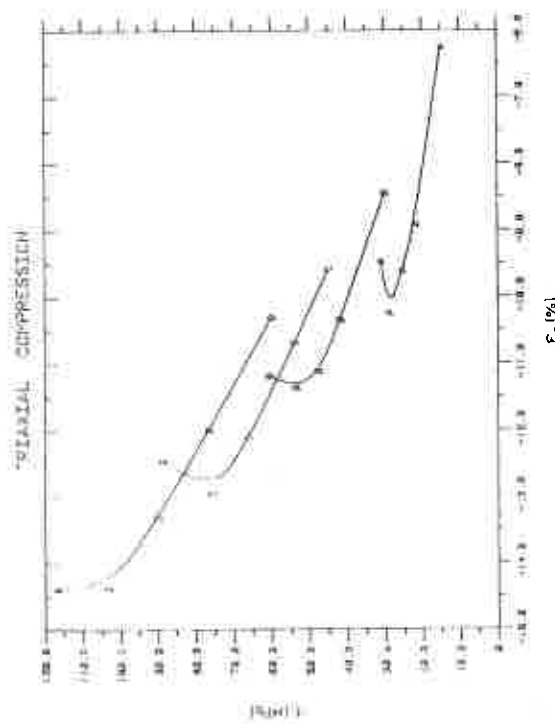
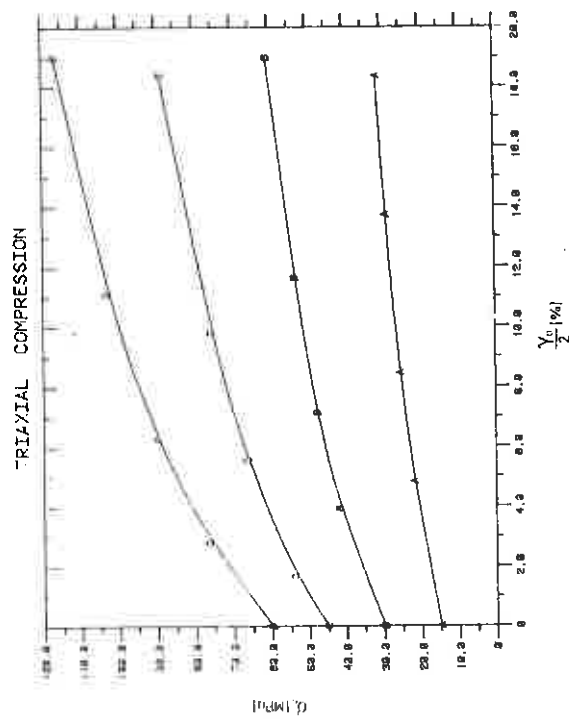


Fig. 17:  $\tau_0$  versus radial strain  $\epsilon_2$



Fig. 19:  $\tau_o$  versus  $\epsilon_o$ Fig. 21:  $\tau_o$  versus  $\delta_o/2$ Fig. 18:  $\sigma_o$  versus  $\epsilon_o$ Fig. 20:  $\sigma_o$  versus  $\delta_o/2$

In Figs. 22-23 we further show the connection between octahedral normal and shearing stresses and the effective plastic strain  $E^*$  (cf. Eq. 3.11).

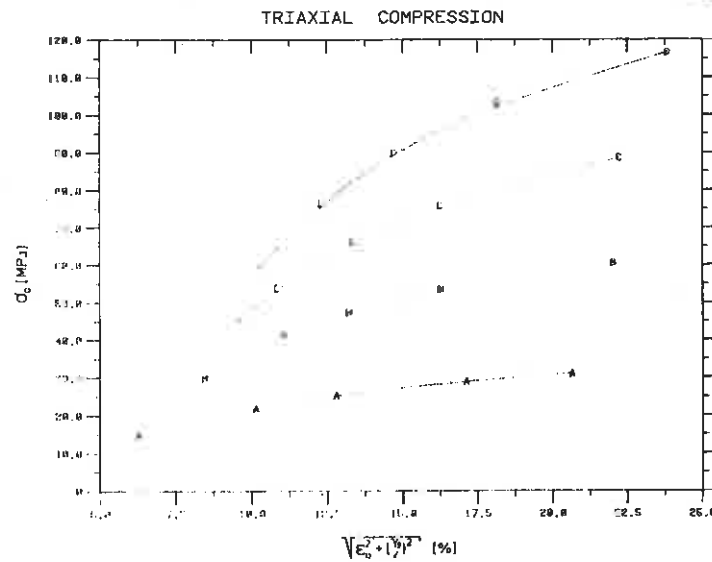


Fig. 22:  $\sigma_0$  versus effective strain  $E^* = \sqrt{\epsilon_0^2 + (\gamma_0/2)^2}$

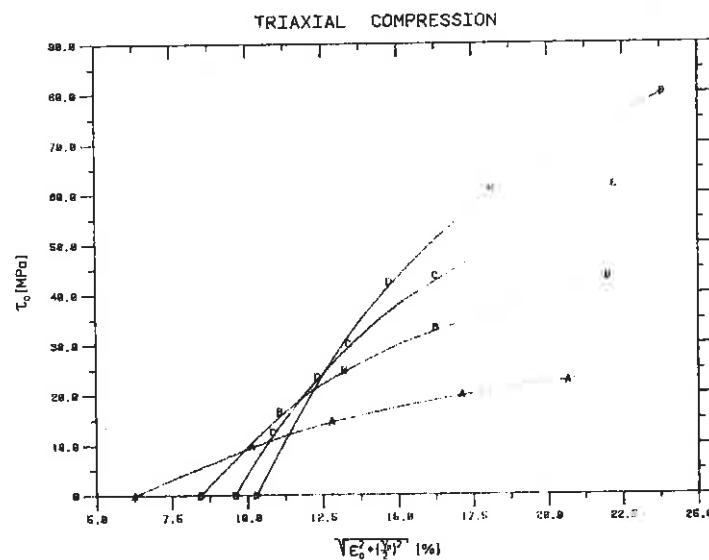


Fig. 23:  $\tau_0$  versus effective strain  $E^* = \sqrt{\epsilon_0^2 + (\gamma_0/2)^2}$

At this point we are ready to show the portions of load surfaces which can be constructed from the available experimental data, which is done in Figs. 24-27.

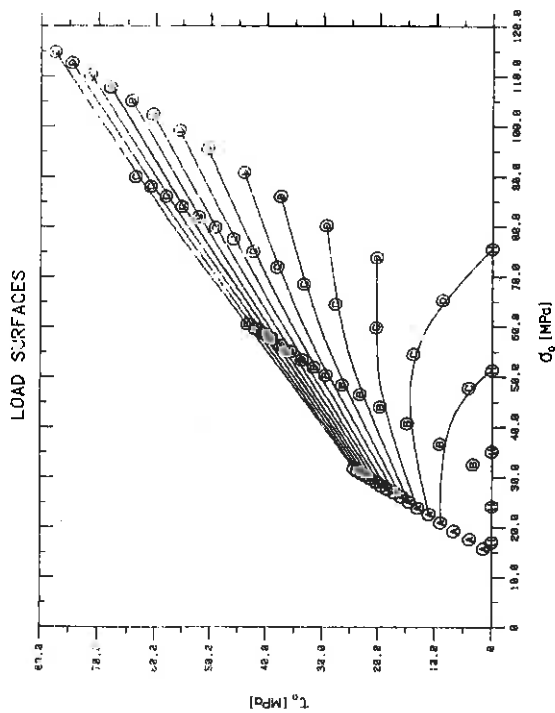


Fig. 24: Load surfaces in octahedral stress plane for  $E = 7, 8, 9, \dots, 23\%$

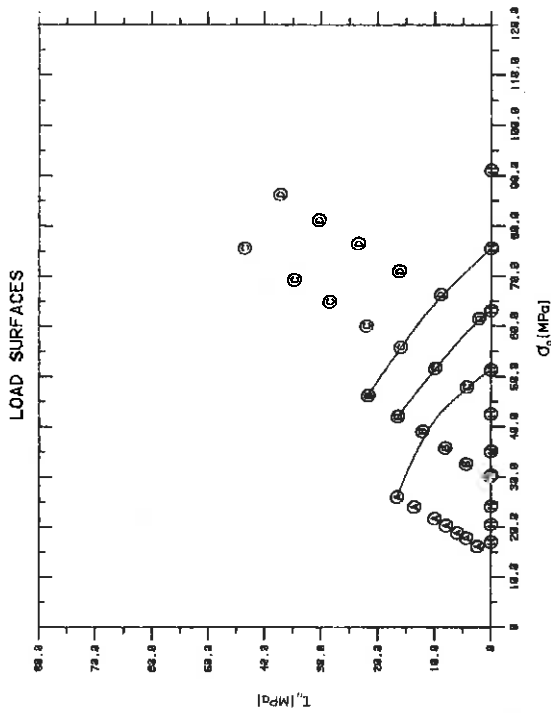


Fig. 26: Load surface in octahedral stress plane for  $E_0 = 7, 7.5, 8, 8.5, \dots, 13\%$

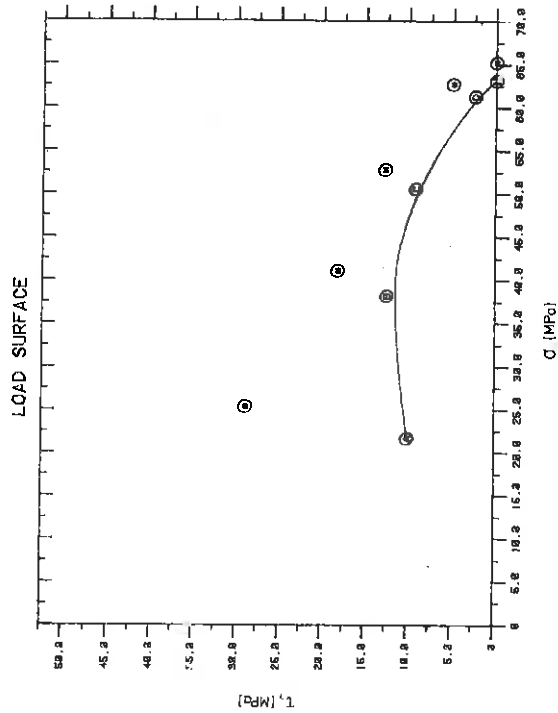


Fig. 25: "Normality of strain increment" for  $\Delta G_1 = 0.5 \text{ MPa}$  and  $E = 10.5\%$ .

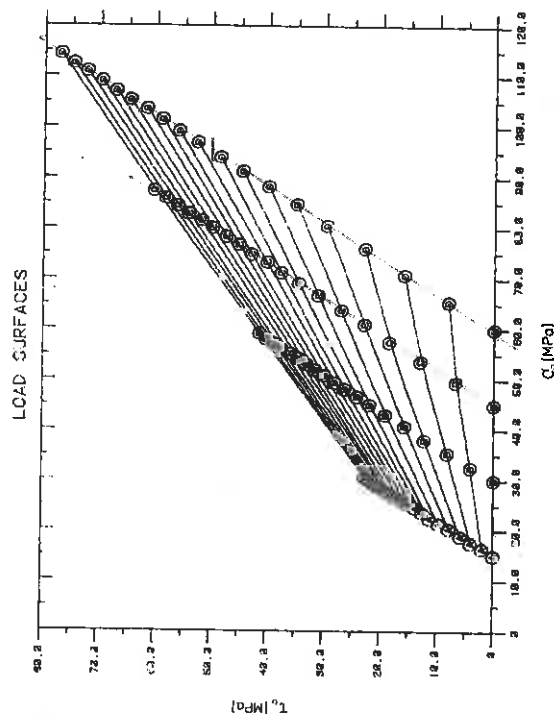


Fig. 27: Load surfaces in octahedral stress plane for  $\epsilon_0/2 = 0, 1, 2, \dots, 18\%$

In Fig. 25 we check the validity of Drucker's postulate [Drucker (1951); Kachanov (1971)] for stable materials, which states that any additional loading  $\Delta \sigma > 0$  will give rise to an additional plastic strain  $\Delta \epsilon^p$  such that the plastic work done is positive and the increment  $\Delta \epsilon^p$  is perpendicular to a tangential plane with respect to the load surface. The asterisks in Fig. 25 visualize the end points of the strain increments such that a  $\Delta \epsilon_0$  of  $\sim 0.01\%$  corresponds to 1MPa in the  $\sigma_0$ -direction and a  $\Delta (\delta_{0/2})$  of 0.01% corresponds to 1MPa in the  $\tau_0$ -direction. The stress increment was taken to be  $\Delta \sigma_1 = 0.5\text{MPa}$  which corresponds to  $\Delta \sigma_0 = \frac{1}{6}\text{MPa}$  and  $\Delta \tau_0 = \frac{\sqrt{2}}{6}\text{MPa}$ . We will comment on various factors influencing the accuracy and reliability of these results in the discussion of section 5 below.

In all load surfaces it is clearly seen that points associated with our given confining pressure (A: 15MPa; B: 30MPa; C: 45MPa; D: 60MPa) lie on straight lines with slope  $\sqrt{2}$ , which is evident from the connection

$$(3.12) \quad \tau_0 = \sqrt{2} \sigma_0 - \sqrt{2} \sigma_2$$

For  $\sigma_2=0$  one obtains the special case of the uniaxial test. Unfortunately, since failure occurs already for  $\sigma_1 \sim 3\text{MPa}$  at  $\delta_{0/2} \sim 0.25\%$ , it is impossible to incorporate the uniaxial results in Figs. 24-27.

#### 4. THEORETICAL STUDIES

##### 4.1 Constitutive relations

##### 4.1.1 Preliminaries

During recent years various constitutive relations for granular materials have been discussed in the literature, see e.g. Desai (1979), DiMaggio and Sandler (1971), Sandler et al (1976) and Nilsson (1979). Most of these relations concern the materials sand, rock and concrete. However, the mechanical behaviour of metal powder can very well be described by any of these relations. The following discussion is restricted to the flow theory of plasticity, since our experimental studies indicate rate independent material behaviour in the range of interest.

There are two main phenomena which our material model must account for:

- (a) nonlinear dilatancy and compaction
- (b) plastic flow, which depends both on deviatoric and volumetric states of stress

To describe these phenomena, we have chosen to separate elastic and plastic states of stress by two loading functions. The theory of multiply segmented loading functions has been developed by Koiter (1953) and may be considered as a part of the classical flow theory of plasticity. The present choice of loading functions follows to some extent Sandler et al (1976) and Green and Swanson (1973).

From our experimental results we conclude that constitutive relations designed to cover hard metal powder must incorporate strains of considerable magnitude ( $>40\%$ ). Hence our analysis must not be restricted to small strains. Convenient frame invariant measures of stress and strain are the Jauman stress rate tensor  $\dot{\sigma}$  and the rate of deformation tensor  $d$ , respectively [see e.g. Malvern (1969)].

These are defined by

$$(4.1) \quad \dot{\tilde{\epsilon}}_{ij} = \dot{\epsilon}_{ij} - \omega_{ik}\epsilon_{kj} - \omega_{jk}\epsilon_{ki}$$

( $\dot{\phantom{x}} \equiv \partial/\partial t$ ) where  $\underline{\epsilon}$  is the Cauchy stress tensor  
and  $\underline{\omega}$  is the spin rate tensor defined by

$$(4.2) \quad \omega_{ij} = \frac{1}{2} (v_{ij} - v_{ji})$$

( $\underline{v}$  being the displacement vector), and

$$(4.3) \quad d_{ij} = \frac{1}{2} (v_{ij} + v_{ji})$$

For infinitesimal deformations  $\tilde{\epsilon} = \underline{\epsilon}$  and  $\dot{\tilde{\epsilon}} = \dot{\underline{\epsilon}}$ , where  $\underline{\epsilon}$  is the small strain tensor. For the sake of simplicity, we will still use small deformation notations in the following. However, we emphasize that finite strains usually are attained in our applications.

#### 4.1.2 Basic tangential stiffness formulation

Following the flow theory of plasticity, we assume that the strain rate tensor  $\dot{\underline{\epsilon}}$  can be decomposed into elastic,  $\dot{\underline{\epsilon}}^e$ , and plastic,  $\dot{\underline{\epsilon}}^p$ , parts, i.e.

$$(4.4) \quad \dot{\epsilon}_{ij} = \dot{\epsilon}_{ij}^e + \dot{\epsilon}_{ij}^p$$

The stress rate components follow from

$$(4.5) \quad \dot{\sigma}_{ij} = S_{ijkl} (\dot{\epsilon}_{kl} - \dot{\epsilon}_{kl}^p)$$

The two segments of our loading function are (assuming initial isotropic material behaviour)

$$(4.6) \quad f_1(\sigma_{ij}, k_1) = f_1(\sigma_o, \tau_o, \theta, k_1(\epsilon_{kl}^p)); \quad \sigma_o \leq \sigma_{oc}$$

$$(4.7) \quad f_2(\sigma_{ij}, k_2) = f_2(\sigma_o, \tau_o, \theta, k_2(\epsilon_{kl}^p)); \quad \sigma_o \geq \sigma_{oc}$$

where  $\sigma_o$  and  $\tau_o$  are the octahedral stresses defined by (3.6) and (3.8),

$$\theta = \{\arccos [\sqrt{2} \sigma'_{ij} \sigma'_{jk} \sigma'_{ki} / (3\tau_o^3)]\} / 3; \quad \sigma'_{ij} = \sigma_{ij} - \frac{1}{3} I_1 \delta_{ij}$$

is the angle of similarity, and  $k_1(\epsilon_{kl}^p)$  and  $k_2(\epsilon_{kl}^p)$  are two hardening or softening functions which account for the material destruction. The Rendulic section of the loading function is shown in Fig. 28.

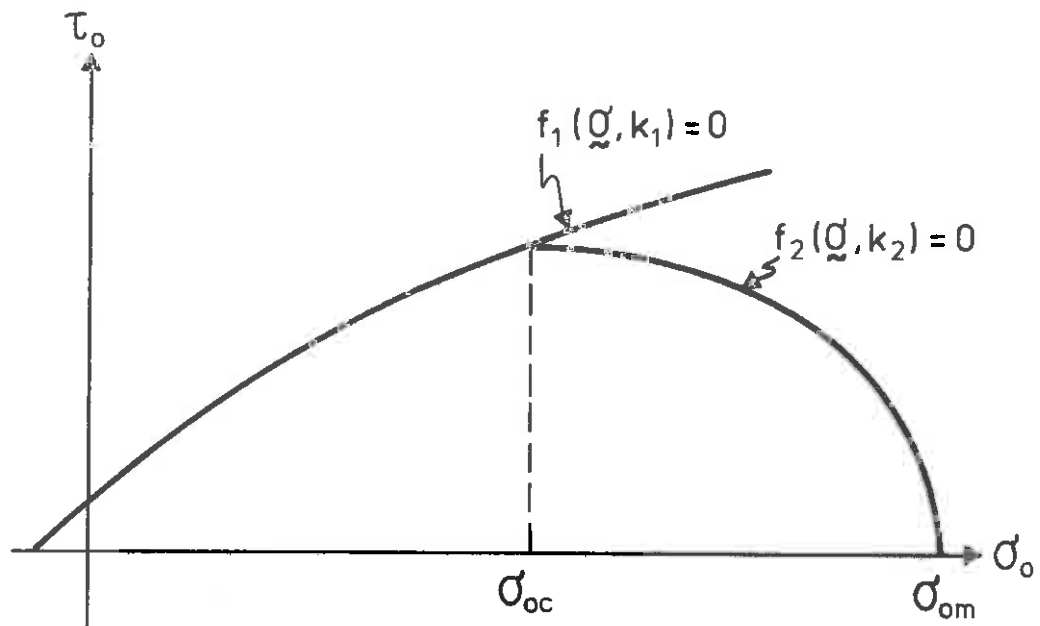


Fig. 28: Two segmented loading surface

Plastic loading occurs if one of the following three conditions is met:

$$(4.8) \quad \begin{cases} f_1(\sigma_{ij}, k_1) = 0 & \text{and} & \dot{f}_1(\sigma_{ij}, k_1) = 0 \\ f_2(\sigma_{ij}, k_2) < 0 \end{cases}$$

$$(4.9) \quad \begin{cases} f_1(\sigma_{ij}, k_1) < 0 \\ f_2(\sigma_{ij}, k_2) = 0 & \text{and} & \dot{f}_2(\sigma_{ij}, k_2) = 0 \end{cases}$$

or

$$(4.10) \quad \begin{cases} f_1(\sigma_{ij}, k_1) = 0 & \text{and} & \dot{f}_1(\sigma_{ij}, k_1) = 0 \\ f_2(\sigma_{ij}, k_2) = 0 & \text{and} & \dot{f}_2(\sigma_{ij}, k_2) = 0 \end{cases}$$

The two conditions (4.8) and (4.9) do not deviate from the ordinary single segmented loading conditions. The condition (4.10) implies that the stress point lies on the intersection of the two surfaces. We will show that the plastic flow from the conditions (4.8) or (4.9) will follow as special cases of the condition (4.10). During the plastic flow, an extended normality rule [Koiter (1953)] is assumed to hold

$$(4.11) \quad \dot{\epsilon}_{ij}^P = \dot{\lambda}_1 \frac{\partial f_1}{\partial \sigma_{ij}} + \dot{\lambda}_2 \frac{\partial f_2}{\partial \sigma_{ij}}$$

From eqs. (4.5) and (4.10 - 11) we obtain

$$(4.12) \quad \begin{aligned} \dot{f}_1 &= \frac{\partial f_1}{\partial \sigma_{ij}} \dot{\sigma}_{ij} + \frac{\partial f_1}{\partial k_1} \frac{\partial k_1}{\partial \epsilon_{ij}^P} \dot{\epsilon}_{ij}^P \\ &= \frac{\partial f_1}{\partial \sigma_{ij}} S_{ijkl}^e (\dot{\epsilon}_{kl} - \dot{\lambda}_1 \frac{\partial f_1}{\partial \sigma_{kl}} - \dot{\lambda}_2 \frac{\partial f_2}{\partial \sigma_{kl}}) + \\ &\quad + \frac{\partial f_1}{\partial k_1} \frac{\partial k_1}{\partial \epsilon_{kl}^P} (\dot{\lambda}_1 \frac{\partial f_1}{\partial \sigma_{kl}} + \dot{\lambda}_2 \frac{\partial f_2}{\partial \sigma_{kl}}) = 0 \end{aligned}$$

and

$$(4.13) \quad \begin{aligned} \dot{f}_2 &= \frac{\partial f_2}{\partial \sigma_{ij}} \dot{\sigma}_{ij} + \frac{\partial f_2}{\partial k_2} \frac{\partial k_2}{\partial \epsilon_{ij}^P} \dot{\epsilon}_{ij}^P \\ &= \frac{\partial f_2}{\partial \sigma_{ij}} S_{ijkl}^e (\dot{\epsilon}_{kl} - \dot{\lambda}_1 \frac{\partial f_1}{\partial \sigma_{kl}} - \dot{\lambda}_2 \frac{\partial f_2}{\partial \sigma_{kl}}) + \\ &\quad + \frac{\partial f_2}{\partial k_2} \frac{\partial k_2}{\partial \epsilon_{kl}^P} (\dot{\lambda}_1 \frac{\partial f_1}{\partial \sigma_{kl}} + \dot{\lambda}_2 \frac{\partial f_2}{\partial \sigma_{kl}}) = 0 \end{aligned}$$

Equations (4.12) and (4.13) can be rewritten in matrix form as

$$(4.14) \quad \begin{bmatrix} A & B \\ C & D \end{bmatrix} \begin{bmatrix} \dot{\lambda}_1 \\ \dot{\lambda}_2 \end{bmatrix} = \begin{bmatrix} E \\ F \end{bmatrix}$$



where

$$\begin{aligned}
 (4.15) \quad A &= \frac{\partial \mathcal{F}_1}{\partial \mathcal{G}_{ij}} S_{ijkl}^e \frac{\partial \mathcal{F}_1}{\partial \mathcal{G}_{kl}} - \frac{\partial \mathcal{F}_1}{\partial k_1} \frac{\partial k_1}{\partial \mathcal{E}_{kl}^p} \frac{\partial \mathcal{F}_1}{\partial \mathcal{G}_{kl}} \\
 B &= \frac{\partial \mathcal{F}_1}{\partial \mathcal{G}_{ij}} S_{ijkl}^e \frac{\partial \mathcal{F}_2}{\partial \mathcal{G}_{kl}} - \frac{\partial \mathcal{F}_1}{\partial k_1} \frac{\partial k_1}{\partial \mathcal{E}_{kl}^p} \frac{\partial \mathcal{F}_2}{\partial \mathcal{G}_{kl}} \\
 C &= \frac{\partial \mathcal{F}_2}{\partial \mathcal{G}_{ij}} S_{ijkl}^e \frac{\partial \mathcal{F}_1}{\partial \mathcal{G}_{kl}} - \frac{\partial \mathcal{F}_2}{\partial k_2} \frac{\partial k_2}{\partial \mathcal{E}_{kl}^p} \frac{\partial \mathcal{F}_1}{\partial \mathcal{G}_{kl}} \\
 D &= \frac{\partial \mathcal{F}_2}{\partial \mathcal{G}_{ij}} S_{ijkl}^e \frac{\partial \mathcal{F}_2}{\partial \mathcal{G}_{kl}} - \frac{\partial \mathcal{F}_2}{\partial k_2} \frac{\partial k_2}{\partial \mathcal{E}_{kl}^p} \frac{\partial \mathcal{F}_2}{\partial \mathcal{G}_{kl}} \\
 E &= \frac{\partial \mathcal{F}_1}{\partial \mathcal{G}_{ij}} S_{ijkl}^e \dot{\mathcal{E}}_{kl} \\
 F &= \frac{\partial \mathcal{F}_2}{\partial \mathcal{G}_{ij}} S_{ijkl}^e \dot{\mathcal{E}}_{kl}
 \end{aligned}$$

The two special cases (4.8) and (4.9) are obtained from equation (4.14) by  $\dot{\lambda}_2 = 0$  and  $\dot{\lambda}_1 = 0$ , respectively. Thus

$$(4.16) \quad \dot{\lambda}_1 = \frac{E}{A} = \frac{1}{A} \frac{\partial \mathcal{F}_1}{\partial \mathcal{G}_{ij}} S_{ijkl}^e \dot{\mathcal{E}}_{kl} \quad (\dot{\lambda}_2 = 0)$$

and

$$(4.17) \quad \dot{\lambda}_2 = \frac{F}{D} = \frac{1}{D} \frac{\partial \mathcal{F}_2}{\partial \mathcal{G}_{ij}} S_{ijkl}^e \dot{\mathcal{E}}_{kl} \quad (\dot{\lambda}_1 = 0)$$

From equations (4.5) and (4.11), we obtain

$$\begin{aligned}
 (4.18) \quad \dot{\mathcal{G}}_{ij} &= S_{ijkl}^e \left\{ \dot{\mathcal{E}}_{kl} - \frac{1}{A} \frac{\partial \mathcal{F}_1}{\partial \mathcal{G}_{rs}} S_{rs mn}^e \dot{\mathcal{E}}_{mn} \frac{\partial \mathcal{F}_1}{\partial \mathcal{G}_{kl}} \right\} \\
 &= \left\{ S_{ijkl}^e - \frac{1}{A} \frac{\partial \mathcal{F}_1}{\partial \mathcal{G}_{rs}} S_{rs kl}^e S_{ij mn}^e \frac{\partial \mathcal{F}_1}{\partial \mathcal{G}_{mn}} \right\} \dot{\mathcal{E}}_{kl} \\
 &\quad (\dot{\lambda}_2 = 0)
 \end{aligned}$$

and

$$\begin{aligned}
 (4.19) \quad \dot{\mathcal{G}}_{ij} &= \left\{ S_{ijkl}^e - \frac{1}{D} \frac{\partial \mathcal{F}_2}{\partial \mathcal{G}_{rs}} S_{rs kl}^e S_{ij mn}^e \frac{\partial \mathcal{F}_2}{\partial \mathcal{G}_{mn}} \right\} \dot{\mathcal{E}}_{kl} \\
 &\quad (\dot{\lambda}_1 = 0)
 \end{aligned}$$

For the case  $\lambda_1 \neq 0$  and  $\lambda_2 \neq 0$  we find from equation (4.14)

$$(4.20) \quad \begin{bmatrix} \dot{\lambda}_1 \\ \dot{\lambda}_2 \end{bmatrix} = \frac{1}{AD - BC} \begin{bmatrix} DE - BF \\ AF - CE \end{bmatrix}$$

From equations (4.5) and (4.11) we obtain

$$(4.21) \quad \begin{aligned} \dot{\sigma}_{ij} &= S_{ijkl}^e \dot{\epsilon}_{kl} - \dot{\lambda}_1 S_{ijkl}^e \frac{\partial \psi_1}{\partial \sigma_{kl}} - \dot{\lambda}_2 S_{ijkl}^e \frac{\partial \psi_2}{\partial \sigma_{kl}} \\ &= \left\{ S_{ijkl}^e - \frac{1}{AD - BC} \left[ \frac{\partial \psi_1}{\partial \sigma_{mn}} D S_{ijmn}^e S_{rskl}^e \frac{\partial \psi_1}{\partial \sigma_{rs}} \right. \right. \\ &\quad \left. \left. - \frac{\partial \psi_1}{\partial \sigma_{mn}} (B S_{ijmn}^e S_{rskl}^e + C S_{ijrs}^e S_{mckl}^e) \frac{\partial \psi_2}{\partial \sigma_{rs}} \right. \right. \\ &\quad \left. \left. + \frac{\partial \psi_2}{\partial \sigma_{mn}} A S_{ijmn}^e S_{rskl}^e \frac{\partial \psi_2}{\partial \sigma_{rs}} \right] \right\} \dot{\epsilon}_{kl} \end{aligned}$$

or

$$(4.22) \quad \dot{\sigma}_{ij} = \underline{S}_{ijkl}^{ep} \dot{\epsilon}_{kl}$$

where  $\underline{S}^{ep}$  is the elastic-plastic tangential stiffness tensor. We notice from equation (4.21) that  $\underline{S}^{ep}$  is unsymmetric for the case  $\dot{\lambda}_1 \neq 0$  and  $\dot{\lambda}_2 \neq 0$ , unless  $B = C$ . This will only happen if

$$(4.23) \quad \frac{\partial \psi_1}{\partial k_1} \frac{\partial k_1}{\partial \epsilon_{kl}^p} \frac{\partial \psi_2}{\partial \sigma_{kl}} = \frac{\partial \psi_2}{\partial k_2} \frac{\partial k_2}{\partial \epsilon_{kl}^p} \frac{\partial \psi_1}{\partial \sigma_{kl}}$$

Thus, in the general case our solution procedure must consider this unsymmetry. For the cases  $\dot{\lambda}_1 \neq 0, \dot{\lambda}_2 = 0$  and  $\dot{\lambda}_2 \neq 0, \dot{\lambda}_1 = 0$  we obtain symmetrical stiffness matrices, c.f. equations (4.18) and (4.19).

#### 4.1.3 On the choice of loading and hardening functions

In order to apply the general theory previously discussed we need explicit expressions for loading and hardening functions. We will assume initial isotropic material behaviour and independence of the angle of similarity. Thus, the loading functions can be completely determined from the mean stress  $\sigma_o$ , the octahedral shear stress  $\tau_o$ , and the hardening functions  $k_1$  and  $k_2$ .

The two loading functions, which we propose, are

$$(4.24) \quad f_1(\sigma_o, \tau_o, k_1) = \tau_o + q(\sigma_o) - k_1(\epsilon_{kl}^p);$$

$\sigma_o \leq \sigma_{oc}$

and

$$(4.25) \quad f_2(\sigma_o, \tau_o, k_2) = \left( \frac{\sigma_o - \sigma_{oc}}{a} \right)^2 + \left( \frac{\tau_o}{b} \right)^2 - 1;$$

$\sigma_o \geq \sigma_{oc}$

where  $\sigma_{oc}$  characterizes the centre of the ellipse. Thus, the function  $q(\sigma_o)$  determines the frictional angle

$$(4.26) \quad \beta = \frac{\partial f_1}{\partial \sigma_o} = \frac{\partial q(\sigma_o)}{\partial \sigma_o}$$

and the functions  $a$  and  $b$  determine the semiaxes of the ellipse.

In the following we assume

$$(4.27) \quad q(\sigma_o) = c_1 e^{-c_2 \sigma_o}$$

where  $c_1$  and  $c_2$  are constants. Furthermore, we define a ratio  $R = a/b$  of the axes of the ellipse.

Thus, we have

$$(4.28) \quad f_1(\sigma_o, \tau_o, k_1) = \tau_o + c_1 e^{-c_2 \sigma_o} - k_1;$$

$$\text{and} \quad \sigma_o \leq \sigma_{oc}$$

$$(4.29) \quad f_2(\sigma_o, \tau_o, k_2) = (\sigma_o - \sigma_{oc})^2 + R^2 \tau_o^2 - [\sigma_{om}(k_2) - \sigma_{oc}]^2;$$

$$\sigma_o \geq \sigma_{oc}$$

where  $\sigma_{om}$  denotes the intersection between the ellipse and the  $\sigma_o$  axes ( $\sigma_o \geq \sigma_{oc}$ ).

The loading function  $f_2(\sigma_o, \tau_o, k_2)$  will in the following be denoted as the "cap". Its intersection with the hydrostatic axis,  $\sigma_{om}$ , is assumed to be governed by the volumetric plastic strain  $\epsilon_o^p = \epsilon_{kk}^p/3$ .

The intersection between the two loading surfaces  $f_1$  and  $f_2$  can be found from the equations

$$(4.30) \quad R c_1 e^{-c_2 \sigma_{oc}} - \sigma_{oc} = \sigma_{om}(\epsilon_o^p) + R k_1 (\epsilon_o^p)$$

and

$$(4.31) \quad \tau_{oc} = \frac{\sigma_{om}(\epsilon_o^p) - \sigma_{oc}}{R}$$

respectively.

From our assumptions it thus follows that  $\sigma_{oc}$  depends both on the volumetric and the deviatoric part of the plastic strain tensor.

DiMaggio and Sandler (1971) propose the following cap hardening relation

$$(4.32) \quad \epsilon_o^p = -W [e^{D(\sigma_{om} - {}^o\sigma_{om})} - 1]$$

or

$$(4.33) \quad \sigma_{om} = \frac{1}{D} [\ln(1 - \epsilon_o^p/W)] + {}^o\sigma_{om}$$

where  $W$  and  $D$  are material constants and  $\sigma_{om}$  is the initial position of the cap.

The constants  $c_1$  and  $c_2$  of the loading function  $f_1$  can be determined from two deviatoric stress paths, e.g. the uniaxial compression test ( $\sigma_o = f/3; \tau_o = \sqrt{2} f/3$ ;  $f$  is the ultimate stress) and the biaxial compression test ( $\sigma_o = 2\alpha f/3; \tau_o = \sqrt{2}\alpha f/3$ ;  $\alpha$  is the ratio biaxial to uniaxial strength).

If we, for simplicity, assume that the metal powder lacks cohesion, we find  $c_1 = k_1$ . Thus, for this case

$$(4.34) \quad c_2 = -\frac{3}{f} \ln [1 - \sqrt{2} f / (3k_1)]$$

Finally, we obtain the constant  $k_1 (y_o^p)$  from the condition  $f_1 = 0; \tau_o \rightarrow k_1$  when  $\sigma_o \rightarrow \infty$ . For simplicity, we assume a linear hardening of the ultimate shear strength.

Thus,

$$(4.32) \quad k_1 = H y_o^p$$

where  $H$  is a material parameter.

#### 4.1.4 Deviation of gradients of the loading functions

In order to establish the tangential stiffness coefficients, we need the gradients of the loading functions  $f_1$  and  $f_2$ . For  $f_1$  we have

$$(4.33) \quad \frac{\partial f_1}{\partial \sigma_{ij}} = \frac{\partial f_1}{\partial \sigma_o} \frac{\partial \sigma_o}{\partial \sigma_{ij}} + \frac{\partial f_1}{\partial \tau_o} \frac{\partial \tau_o}{\partial \sigma_{ij}}$$

With

$$(4.34) \quad \frac{\partial \sigma_o}{\partial \sigma_{ij}} = \delta_{ij}/3$$

and

$$(4.35) \quad \frac{\partial \tau_0}{\partial \sigma_{ij}} = \frac{\sigma_{ij}'}{3\tau_0}$$

we find

$$(4.36) \quad \frac{\partial f_1}{\partial \sigma_{ij}} = c_1 c_2 e^{c_2 \sigma_0} \frac{\sigma_{ij}}{3} + \frac{\sigma_{ij}'}{3\tau_0}$$

$$(4.37) \quad \frac{\partial f_1}{\partial \epsilon_{ij}^P} = \frac{\partial f_1}{\partial k_1} \frac{\partial k_1}{\partial \gamma_0^P} \frac{\partial \gamma_0^P}{\partial \epsilon_{ij}^P}$$

With

$$(4.38) \quad \frac{\partial \gamma_0^P}{\partial \epsilon_{ij}^P} = 4 (\epsilon_{ij}^P)' / (3\gamma_0^P)$$

we obtain

$$(4.38) \quad \frac{\partial f_1}{\partial \epsilon_{ij}^P} = -4H (\epsilon_{ij}^P)' / (3\gamma_0^P)$$

Similarly, we obtain for  $f_2$

$$(4.39) \quad \frac{\partial f_2}{\partial \sigma_{ij}} = \frac{\partial f_2}{\partial \sigma_0} \frac{\partial \sigma_0}{\partial \sigma_{ij}} + \frac{\partial f_2}{\partial \tau_0} \frac{\partial \tau_0}{\partial \sigma_{ij}}$$

or, with (4.34) and (4.35),

$$(4.40) \quad \frac{\partial f_2}{\partial \sigma_{ij}} = \frac{2}{3} (\sigma_0 - \sigma_{oc}) \delta_{ij} + \frac{2}{3} R^2 \sigma_{ij}'$$

Furthermore,

$$(4.41) \quad \frac{\partial f_2}{\partial \epsilon_{ij}^P} = \left\{ \frac{\partial f_2}{\partial \sigma_{om}} + \frac{\partial f_2}{\partial \sigma_{oc}} \frac{\partial \sigma_{oc}}{\partial \sigma_{om}} \right\} \frac{\partial \sigma_{om}}{\partial \epsilon_0^P} \frac{\partial \epsilon_0^P}{\partial \epsilon_{ij}^P} +$$

$$+ \frac{\partial f_2}{\partial \sigma_{oc}} \frac{\partial \sigma_{oc}}{\partial \gamma_0^P} \frac{\partial \gamma_0^P}{\partial \epsilon_{ij}^P}$$

where

$$(4.42) \quad \frac{\partial \epsilon_0^P}{\partial \epsilon_{ij}^P} = \frac{\delta_{ij}}{3}$$

As noticed from equation (4.30), there is no obvious solution for  $\bar{\sigma}_{oc}$ . We therefore propose to solve  $\bar{\sigma}_{oc}$  numerically from equation (4.30), using an iterative technique:

$$(4.43) \quad \bar{\sigma}_{oc}^{(2)} = -\left\{ \ln \left[ (\bar{\sigma}_{om} + Rk_1 - \bar{\sigma}_{oc}^{(1)}) / Rc_1 \right] \right\} / c_2$$

where  $\bar{\sigma}_{oc}^{(1)}$  and  $\bar{\sigma}_{oc}^{(2)}$  denote the first and second estimates of  $\bar{\sigma}_{oc}$ , respectively.

To obtain an approximation of the gradient  $\partial \bar{\sigma}_{oc} / \partial \bar{\sigma}_{om}$  we solve numerically  $\Delta \bar{\sigma}_{oc} / \Delta \bar{\sigma}_{om}$  for a given  $\bar{\sigma}_{oc}$  and  $\Delta \bar{\sigma}_{om}$ :

$$(4.44) \quad \Delta \bar{\sigma}_{oc} = Rc_1 e^{-c_1 \bar{\sigma}_{oc}} \left( e^{-c_2 \Delta \bar{\sigma}_{oc}} + 1 \right) + \Delta \bar{\sigma}_{om}$$

Again, we must use an iterative approach. Thus, equation (4.41) can be rewritten

$$(4.45) \quad \frac{\partial f_2}{\partial \epsilon_{ij}^p} = \left\{ -2(\bar{\sigma}_{om} - \bar{\sigma}_{oc}) + 2(\bar{\sigma}_{om} - \bar{\sigma}_o) \frac{\partial \bar{\sigma}_{oc}}{\partial \bar{\sigma}_{om}} \right\} X \\ \times \frac{1}{DW} \frac{1}{\epsilon_o^p / W - 1} \delta_{ij} / 3 + \frac{8(\bar{\sigma}_{om} - \bar{\sigma}_o) \frac{\partial \bar{\sigma}_{oc}}{\partial \gamma_o^p} (\epsilon_{ij}^p)'}{3\gamma_o^p}$$

where the gradient  $\partial \bar{\sigma}_{oc} / \partial \gamma_o^p$  is computed similarly to  $\partial \bar{\sigma}_{oc} / \partial \bar{\sigma}_{om}$ .

## 4.2 Frictional relations

Due to the discontinuity in material properties, sliding can occur between the powder compact and the surrounding die wall. The mechanical behaviour of this sliding can in general not be derived from the constitutive relations of the contacting materials. The general approach to formulate the sliding relation is based on macroscopically observed phenomena. In this report we will limit our discussion to a simple generalization of the classical Coulomb's frictional law. More detailed discussions can be found in Strijbos (1977), Strijbos et al (1977), Fredriksson (1976), and Nilsson (1979).

Sliding is assumed to occur when

$$(4.46) \quad g(\underline{t}_s, t_n, \mu) = (\underline{t}_s \cdot \underline{t}_s)^{1/2} - \mu t_n$$

where  $\underline{t}_s = [t_{s1}, t_{s2}]^T$  is the vector of tangential contact forces,  $t_n$  is the normal pressure, and  $\mu$  is the angle of friction. The sliding condition (4.46) constitutes a surface (a cone) in the  $(\underline{t}_s, t_n)$  space, c.f. Fig. 29. We assume a non-associated slide rule. Thus, the increments in slip,  $d\underline{r}_s$  and  $dr_n$ , are obtained from

$$(4.47) \quad \begin{cases} dr_{s\alpha} = d\lambda \partial g / \partial t_{s\alpha} ; & \alpha = 1, 2 \\ dr_n = 0 \end{cases}$$

This sliding rule neglects the possible separation between the powder compact and the die wall. However, this separation is assumed to be very small in most practical compact situations.



The increment in dissipative work  $dW_s$  conducted during an incremental sliding is

$$(4.48) \quad dW_s = \underline{t}_s \cdot d\underline{r}_s = t_{s1} dr_{s1} + t_{s2} dr_{s2} \\ = \mu t_n (d\underline{r}_s \cdot d\underline{r}_s)^{1/2}; \quad t_n > 0$$

i.e.

$$(4.49) \quad d\lambda = (d\underline{r}_s \cdot d\underline{r}_s)^{1/2}$$

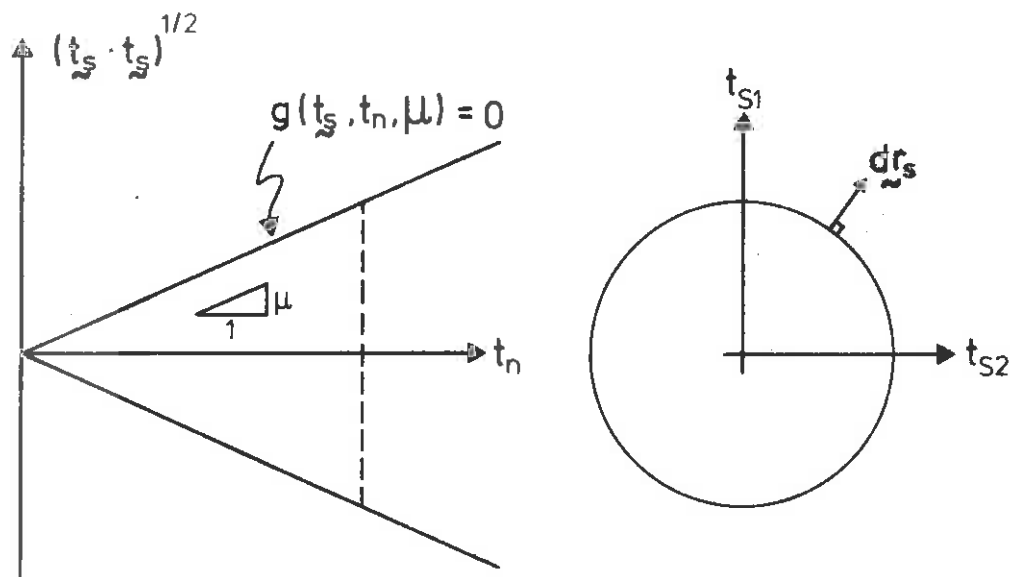


Fig. 29: A generalized Coulomb's sliding surface.

From eq. (4.48) we also obtain

$$(4.50) \quad t_{s\alpha} = \frac{\partial (dW_s)}{\partial (dr_{s\alpha})} = \mu t_n \frac{dr_{s\alpha}}{(d\underline{r}_s \cdot d\underline{r}_s)^{1/2}}; \quad \alpha = 1, 2; \quad t_n > 0$$

In general, the angle of friction is a function of the effective slip, the contact pressure, etc., [see e.g. Strijbos (1977) and Strijbos et al (1977)]. A more detailed investigation of the frictional effects during powders compaction has just been initiated, and will be reported in a forthcoming paper.

#### 4.3 Computational aspects

We have decided to use the FEM - Program ADINA [Bathe, K-J (1978)] for the computational part of our study. ADINA can handle non-linearities of both material and geometric type, but may still be considered as a research program of manageable size. This is important, since we have to implement our own material model for powder material, along with modifications to describe the friction between powder and die wall.

ADINA runs both on the CDC computer of Luleå University and on the IBM 3032 computer at SANDVIK computing center, Sandviken. Program development and testing can therefore be carried out at both places. It is, however, planned to use only the SANDVIK facilities for production runs. The department of process development, SANDVIK Stockholm, which is supervising all basic powder compaction projects, has further access to a Tektronix FEM181 interactive graphics system which can be used for pre- and post-processing of finite element data.

Due to the complexity of the full problem to be solved numerically, we have decided to proceed in four steps:

- (i) Run ADINA for the hydrostatic and triaxial load cases discussed in section 3.1, i.e. for cylindrical test specimens; use axisymmetric two-dimensional elements and try to fit the parameters of the standard Drucker-Prager material model with cap [Drucker and Prager (1952)] to the experimental results.
- (ii) Implement the material model discussed in section 4.1 and recalculate the load cases worked out in (i).

(iii) Treat tool compaction by adding frictional relations at the boundaries in order to account for the friction between powder and die wall. Adjust frictional parameters to experiment.

(iv) Extend the treatment to three dimensions and complicated geometries.

Further details and results will be reported in a forthcoming paper.

## 5. DISCUSSION AND CONCLUSION

Much of the work reported in this paper is preliminary in character. The experiments should rather be termed "pilot tests" and the calculations carried out so far have been of an exploratory nature.

However, the experimental difficulties posed by the extremely large strains during compaction could be overcome in a rather satisfactory way and extensions of the techniques to even larger stresses and strains are under way. After completion of the present modification work we will be able to handle loads twice as high as the ones discussed in this paper. We will then have to concentrate even more on the elimination of some factors which seem to have a negative effect on the accuracy of our measurements.

A first important point is the elimination of variations in the initial density of the test specimens. Ideally it would be desirable to start with the powder itself which, however, is impossible because of practical difficulties with the test equipment: Our triaxial measurements require solid specimens of cylindrical shape and a reasonable accuracy in shaping such cylinders can first be obtained for a minimal hydrostatic compaction pressure of 10 MPa. Therefore we are investigating hard metal powder compacted to a relative density of more than 40%, whereas the relative density of loose powder lies around 25%.

We still believe that the resultant incompleteness of information can be compensated through suitable extrapolation of results for higher degrees of compaction. If the load surfaces for powder material precompacted to, say, 10, 20, 30...MPa were known, it would be possible to predict the behaviour for, say, 5 MPa.

So far we have carried out measurements to construct a significant part of the 10 Mpa - family of load surfaces. Major sources of errors in the quoted results are variations of up to 5% in the initial relative density, slight variations in the confining pressures during the triaxial tests, and also end effects due to friction between the test specimens and the stamps of the triaxial cell. By inspecting the figures it can be stated, however, that the irregularities due to such errors only had an insignificant effect on the overall shape of the load surfaces which came out roughly as anticipated from our study of previous investigations of granular materials.

By studying the constructed load surfaces it becomes apparent that the mean stress has a great influence on the plastic flow. However, the definition of effective plastic strain (distorsion measure) is not a straightforward matter. Thus, when using the effective plastic strain  $E^*$ , we do not generally obtain normality between the plastic strain increments and the load surfaces. Further studies on the choice of effective plastic strain measures are warranted.

In conclusion, it remains to be seen how well the model outlined in section 4.1 will reproduce our test data and how well it will carry over to a description of tool pressing, which also requires a reasonably accurate modelling of the friction between powder compact and die wall.

6. REFERENCES

- ALM, O. (1976), Thermal Conductivity of Insulating Solids Under Pressure, Doctoral Thesis, Department of Physics, University of Umeå, p. 43
- ANTES, H.W. (1970), "Cold Forging Iron and Steel preforms", 1970 International Conference on Powder Metallurgy
- ARZT, E. and H.F.FISCHMEISTER (1979), Fundamental Aspects of the Compaction of Metal Powders, Colloque sur la Compression des Poudres Métalliques, Paris 15.3 1979
- BALSHIN, M.Y. (1938), Theory of Compacting, Metallogram, Vol. 18, p. 124
- BATHE, K-J (1978), ADINA - A finite element program for Automatic Dynamic Incremental Nonlinear Analysis, MIT Report 82448-1
- BOCKSTIEGEL, G. and J. HEWING (1965), Kritische Betrachtung des Schrifttums über den Verdichtungsvorgang beim Kaltpressen von Pulvern in starren Pressformen, Arch. Eisenhüttenwes. 36, p. 751-767
- BROESE VAN GROENOU, A. (1978), Pressing of Ceramic Powders: A Review of Recent Work, Powder Met. Internat. 10, 206-211
- BROESE VAN GROENOU, A. (1980), Compaction of Ceramic Powders, Proceedings from European Symp. on Particle Technology, June 3-5 1980, Amsterdam, Holland

- BROESE VAN GROENOU, A. and A.C. KNAAPEN (1980),  
Density Variations in Die-Compacted Powders,  
Sc. of Ceramics 10 (in press)
- CUNDALL, P.A. and O.D.L. Strack (1979), A Discrete  
Numerical Model for Granular Assemblies,  
Géotechnique 29, No. 1, p. 47-65
- DESAI, C.S. (1979), Some Aspects on Constitutive  
Models for Geological Media, Proceedings of  
the Third International Conference on Numerical  
Methods in Geomechanics, Aachen (A.A. Balkema,  
Rotterdam) Vol. 1. p. 299-308
- DI MAGGIO, F.L. and I.S. SANDLER (1971), Material  
Model for Granular Soils, Journal of the  
Engineering Mechanics Division, ASCE, Vol.97.  
No. EM3, Proc. Paper 8212, p. 935-950
- DRUCKER, D.C. (1951), A More Fundamental Approach to  
Plastic Stress-Strain Relations, Proc. of the  
1st US Natl. Congr. of Appl. Mech. (ASME) 79,  
pp 487-491
- DRUCKER, D.C. and W. PRAGER (1952), Soil Mechanics  
and Plastic Analysis or Limit Design, Quart.  
Appl. Math. 10, 2, p. 157-165
- FISCHMEISTER, H.F., E. ARZT and L.R. OLSSON (1978),  
Powd. Metall. 4, p. 179
- FREDRIKSSON, B. (1976), On Elastostatic Contact Problems  
with Friction, Diss. No. 6, Linköping University
- GREEN, S.J. and S.R. SWANSON (1973), Static  
Constitutive Relations for Concrete, Technical  
Report No. AFWL-TR-72-2 (U.S. Air Force Weapons  
Laboratory)

- HECKEL, R.W. (1961), Density-Pressure Relationships in Powder Compaction, Trans. Metall. Soc. AIME, Vol. 221. p. 671
- HEWITT, R.L., W. WALLACE and M.C. DE MALHERBE (1973), The Effects of Strain Hardening in Powder Compaction, Powd. Metall. 16, No. 31
- HEWITT, R.L., R. VENTER and M.C. DE MALHERBE (1973), Theories Relating to the Compaction of Metal Powders, The South African Mechanical Engineer 23, p. 214-222
- KACHANOV, L.M. (1971), Foundations of the Theory of Plasticity, North-Holland, Amsterdam
- KOITER, W.T. (1953), Stress-Strain Relations, Uniqueness and Variational Theorems for Elastic-Plastic Materials with a Singular Yield Surface, 2. Appl. Math. 11, pp. 350-354
- KONOPICKY, K. (1948), Parallelität der Gesetzmäßigkeiten in Keramik und Pulvermetallurgie, Radex-Rundschau, Vol. 1. p. 141
- KUHN, H.A. and C. DOWNEY (1971), Deformation Characteristics and Plasticity Theory of Sintered Powder Materials, Int. J. of Powd. Metall. 7 (1), p. 15
- MALVERN, L.E. (1969), Introduction to the Mechanics of a Continuous Medium, Prentice-Hall, Inc., Englewood-Cliffs, N.J.



- MEERMAN, W.C.P.M., and A.C. KNAAPEN (1979), A High-Pressure Triaxial Testing Cell, Powder Technol. 22 p. 271-278
- NILSSON, L. (1979), Impact Loading on Concrete Structures, Chalmers University of Technology, Department of Structural Mechanics, Publication 79:1
- SANDLER, I.S., F.L. DI MAGGIO and G.Y. BALADI (1976), Generalized Cap Model for Geological Materials, Journal of the Geotechnical Engineering Division, ASCE, Vol. 102, No. GT7, p. 683-699
- SHAPIRO, I. and I.M. KOLTHOFF (1947), The Compressibility of Silver Bromide Powders, Vol. 51, p. 483
- SJÖBERG, G., V. MIRDNOV and H.F. FISCHMEISTER (1977), Powd. Metall. Int. 9, p. 160
- STRIJBOS, S., A. BROESE VAN GROENOU and P.A. VERMEER (1979), Recent Progress in Understanding Die Compaction of Powders, J. Am. Ceram. Soc. 62, p. 57-59
- STRIJBOS, S., P.J. RANKIN, R.J. KLEIN WASSINK, J. BANNINK and G.J. OUDEMANS (1977), Stresses Occurring During One-Sided Die Compaction of Powders, Powder Technol. 18, p. 187-200
- STRIJBOS, S. (1977), Powder-Wall Friction: The Effects of Orientation of Wall Grooves and Wall Lubricants, Powder Technol. 18, p. 209-214

- SUH, N.P. (1969), A Yield Criterion for Plastic, Fractional, Work-hardening Granular Materials, Int. J. of Powd. Metall. 5 (1), p. 69
- TORRE, C (1948), Berg-u. Hüttenmänn. Motatsh. 93, p. 62
- WALKER, E.E. (1923), The Compressibility of Powder, Trans. Faraday Soc., Vol. 19, p. 83
- VERMEER, P.A. (1980), Formulation and Analysis of Sand Deformation Problems, Report No. 195 of the Geotechnical Laboratory, Delft University of Technology
- ZIENKIEWICZ, O.C. (1977), The Finite Element Method, (3rd edition), McGraw-Hill, London